

THE MID-INFRARED EMISSION OF NARROW-LINE ACTIVE GALACTIC NUCLEI: STAR-FORMATION, NUCLEAR ACTIVITY AND TWO POPULATIONS REVEALED BY WISE

DAVID J. ROSARIO, LEONARD BURTSCHER, RICHARD DAVIES, REINHARD GENZEL, DIETER LUTZ, LINDA J. TACCONI
Max Planck Institute for Extraterrestrial Physics, Postfach 1312, 85741 Garching, Germany
Draft version October 30, 2018

ABSTRACT

We explore the nature of the long-wavelength mid-infrared (MIR) emission of a sample of 13000 local Type II (narrow-line) Active Galactic Nuclei (AGNs) from the Sloan Digital Sky Survey (SDSS) using 12 and 22 μm photometry from the WISE all-sky survey. In combination with FIRST 1.4 GHz photometry, we show that AGNs divide into two relatively distinct populations or “branches” in the plane of MIR and radio luminosity. Seyfert galaxies lie almost exclusively on a MIR-bright branch (Branch A), while low-ionization nuclear emission line galaxies (LINERs) are split evenly into Branch A and the MIR-faint Branch B. We devise various tests to constrain the processes that define the branches, including a comparison to the properties of pure star-forming (SF) inactive galaxies on the MIR-Radio plane. We demonstrate that the total MIR emission of objects on Branch A, including most Seyfert galaxies, is governed primarily by host star-formation, with $\approx 15\%$ of the 22 μm luminosity coming from AGN-heated dust. This implies that on-going dusty star-formation is a general property of Seyfert host galaxies. We show that the 12 μm broad-band luminosity of AGNs on Branch A is suppressed with respect to star-forming galaxies, possibly due to the destruction of PAHs or deeper 10 μm Si absorption in AGNs. We uncover a correlation between the MIR luminosity and [O III] $\lambda 5007$ luminosity in AGNs. This suggests a relationship between the SFR and nuclear luminosity in the AGN population, but we caution on the importance of selection effects inherent to such AGN-dominated emission-line galaxies in driving such a correlation. We highlight the MIR-radio plane as a useful tool in comparative studies of SF and nuclear activity in AGN.

1. INTRODUCTION

Through their enormous and concentrated energetic output, supermassive black holes (SMBHs) are expected to play an important role in the evolution of their host galaxies. As yet elusive is a detailed understanding of the interplay between accretion onto the black hole and their final output. Recently, patterns exhibited by stellar mass black holes have been shown to extend to their supermassive cousins, allowing various relationships to be proposed between the accretion rate, radiative efficiency and mechanical output via relativistic outflows (e.g. Maccarone et al. 2003; Merloni et al. 2003; Churazov et al. 2005; Trump et al. 2011). At low specific accretion rates (Eddington ratios $\lambda_E \lesssim 10^{-2}$), the flow onto the SMBH is believed to be radiatively inefficient, possibly advecting much of its thermal energy through the event horizon. A substantial fraction of the accreted mass is channeled into radio-emitting jets, likely mediated by the magnetic field of the SMBH. At higher λ_E , the accretion flow settles into a radiatively efficient thin disk, which produces a profuse X-ray and extreme ultra-violet (EUV) radiation field at the expense of the relativistic outflow. The bright high-energy spectrum of such an AGN can strongly ionize gas out to kiloparsecs, resulting in extended AGN emission line regions.

In most AGNs, the direct EUV is inaccessible due to its high optical depth to gas and dust from the vicinity of the SMBH and on galaxy scales. Much of the absorbed EUV is reprocessed to the mid-infrared (MIR) from AGN-heated dust, at hundreds of K, located in the putative pc-scale “torus”. Indeed, AGN spectral energy distributions (SEDs) show clear evidence for excess hot

dust in the MIR (e.g. Sanders et al. 1989; Netzer et al. 2007; Wu et al. 2009). Therefore, the relative output of an AGN between the MIR and radio wavelengths may serve as a tracer of the accretion mode of the growing SMBH.

There is, however, an important complication to this simple argument. The emission of galaxies in the MIR is also influenced by other processes, most importantly the heating of very small dust grains by star-formation (SF) and evolved stellar populations (e.g. Rowan-Robinson & Crawford 1989; Desert et al. 1990; Draine & Li 2001; Groves et al. 2012), as well as the excitation of the complex of bands from Polycyclic Aromatic Hydrocarbons (PAHs) (e.g. Draine & Li 2007). Prior to an investigation of the accretion properties of AGNs, an account must be made for the MIR emission from these other processes. Such an approach also affords a worthwhile by-product. The thermal infrared is a valuable tracer of star-formation and is relatively free of the effects of extinction or optical depth saturation that affects the UV or optical emission lines (e.g. Calzetti et al. 2007). In massive, metal-rich galaxies, such as AGN hosts, most of the emission from young stars is reprocessed by dust in molecular clouds and emitted in the IR. Therefore, a detailed study of the MIR in AGNs can provide a handle on both the accretion properties of the nuclear source and its relationship to SF in the host galaxy.

Theoretical and empirical arguments support a connection between SF and nuclear activity in AGN hosts, either by direct synchronization between a starburst and the fueling of the nucleus (Sanders et al. 1988; Norman & Scoville 1988; Storchi-Bergmann et al. 2001; Davies et al. 2007), or indirectly mediated by the avail-

ability of cold gas needed for luminous AGN activity (Heller & Shlosman 1994; Rosario et al. 2013). In the era of the Infrared Space Observatory (ISO) and the Spitzer space telescope, much work has examined the interplay between AGN and SF through the use of MIR spectroscopy (Genzel & Cesarsky 2000; Verma et al. 2005; Soifer et al. 2008), employing fine structure emission lines of various ionized species (e.g. Genzel et al. 1998; Sturm et al. 2002; Meléndez et al. 2008; Tommasin et al. 2010; Diamond-Stanic & Rieke 2012), PAH features and their relative strengths (e.g. Schweitzer et al. 2006; Shi et al. 2007; O’Dowd et al. 2009; Diamond-Stanic & Rieke 2010; LaMassa et al. 2012), and continuum luminosities and MIR colors (e.g. Wu et al. 2009; LaMassa et al. 2010). These studies have greatly enhanced our understanding of the MIR phenomenology and physics relevant to the AGN-SF connection, firming up such results as the increased abundance of AGN signatures in IR-luminous galaxies (e.g. Genzel et al. 1998; Nardini et al. 2008), the anticorrelation of PAH strength with AGN prominence (e.g. Clavel et al. 2000; O’Dowd et al. 2009; LaMassa et al. 2010) and the greater depth of the 10 μm Si absorption feature in Type II AGNs (e.g. Shi et al. 2006; Hao et al. 2007). However, as discussed in Section 2.2.2, most of these studies were limited to either very nearby or fairly luminous systems, selected based on the capabilities of the early Infrared Astronomical Satellite (IRAS) (Soifer et al. 1987; Rush et al. 1993).

A recent huge leap forward comes from the surveys from the Wide-field Infrared Survey Explorer (WISE), with more than two orders of magnitude deeper MIR sensitivity than IRAS over the whole sky, enabling a greater dynamic range and better photometry of sources over a wider range of redshifts. In this paper, we use MIR and radio photometry from the WISE and FIRST surveys to assess the dominant source of the total, galaxy-integrated MIR emission in local ($z < 0.15$) narrow emission line-selected AGNs from the SDSS. The data and sample properties are laid out in Section 2. In Section 3, we discuss the diagnostics of the MIR-radio luminosity plane and outline two distinct populations of AGNs, which we discuss in the context of AGN ionization classes. We perform various tests using ancillary measurements from the SDSS and AKARI surveys (Section 4) and then synthesize our findings towards an understanding of the nature of the two populations (Section 5).

Throughout this work, we assume a Λ -CDM Concordance cosmology with $H_0 = 73 \text{ km s}^{-1} \text{ Mpc}^{-1}$ and $\Omega_\Lambda = 0.7$.

2. SAMPLE SELECTION AND DATA

2.1. SDSS Emission-Line AGNs

Emission line-selected AGNs were drawn from the MPA-JHU database of spectral measurements, based on the Sloan Digital Sky Survey (SDSS) Data Release 7 (DR7, Abazajian et al. 2009). This database is restricted to objects with galaxy-like spectra and narrow Balmer lines, specifically excluding broad-line (Type I) AGNs. Therefore, our sample consists almost exclusively of narrow-line (Type II) AGNs. From the entire catalog of 818333 unique galaxies, we chose all objects satisfying the following criteria:

- A high-quality spectroscopic redshift in the range $0.02 < z < 0.15$.
- $S/N > 3$ in the emission lines of $[\text{O III}]\lambda 5007$, $\text{H}\beta$, $\text{H}\alpha$ and $[\text{N II}]\lambda 6584$, as well as a $S/N > 2$ in the weaker $[\text{S II}]\lambda 6720$ line doublet.
- A location in the standard ‘BPT’ diagram of $[\text{O III}]\lambda 5007/\text{H}\beta$ vs. $[\text{N II}]\lambda 6584/\text{H}\alpha$ (Baldwin et al. 1981; Veilleux & Osterbrock 1987) above the curve which separates objects with AGN-dominated ionization from composite and SF galaxies (Kewley et al. 2001, 2006). These are objects in the Seyfert and LINER domains of the BPT diagram.
- Equivalent width of $\text{H}\alpha > 3\text{\AA}$ to ensure that weak LINERs are excluded from the sample. Lines in systems with weaker $\text{H}\alpha$ can arise primarily in shocks or through the UV field from evolved stars, rather than by a nuclear source (Cid Fernandes et al. 2011).

From this subset of 13339 AGNs, we separated high-ionization AGN (Seyferts) from LINERs using the $[\text{S II}]\lambda 6720/\text{H}\alpha$ criterion of Kewley et al. (2006), Eqns. 7 & 12. The use of a simple cut in $[\text{O III}]\lambda 5007/\text{H}\beta$ ratio of 3.0 to separate high and low ionization AGNs leads to considerable mixing at the boundaries of these populations in the standard BPT diagram. Hence, we adopted the use of the fainter $[\text{S II}]$ line as an additional selection criterion, even though it tends to reject intrinsically lower luminosity AGNs with faint emission line fluxes.

We also make use of host stellar mass (M_*) and 4000 \AA break ($D_n 4000$) measurements from the MPA-JHU database. The masses were derived from fits to the five-band SDSS photometry of the hosts, following the methodology of Salim et al. (2007). The procedure for $D_n 4000$ measurements is described in Kauffmann et al. (2003a).

2.1.1. Selection effects inherent to SDSS emission line-selected AGNs

AGNs selected through BPT-based criteria from the SDSS spectroscopic database give us by far the largest census of local nuclear activity. While a remarkable resource for AGN studies, a finer understanding of the relationship between AGN activity and the properties of host galaxies requires an appreciation of the biases inherent to the selection of such AGN samples.

Standard BPT criteria divide emission-line galaxies into three populations: AGN-dominated, SF-dominated and so-called ‘composite’ systems. The last category includes objects that show line ratios intermediate to SF- and AGN-dominated systems, and contain a large number of AGNs with substantial SF in their inner regions (e.g. Kauffmann et al. 2003b; Juneau et al. 2011). AGN-dominated systems, those which lie above the curve from Kewley et al. (2001), have their line emission from within the SDSS aperture largely arising in AGN ionized gas. While cleanly separating out AGNs, this criterion additionally selects against objects with strong star-formation in the central aperture. AGN-dominated systems will have, on average, a lower SFR within the SDSS aperture than purely SF or composite systems.

The SDSS aperture (3" is diameter) covers between 0.6 and 3.8 kpc (projected) in galactic radius across our working redshift range of 0.02–0.15. This may be compared to the typical effective radii of massive galaxies, which range from 2–8 kpc (Trujillo et al. 2006). In general, the SDSS aperture covers less than half of a galaxy’s light. The typical size of the Narrow-Line Region (NLR), in which most of the AGN-ionized emission originates, is ~ 1 kpc for bright Seyfert galaxies (Bennert et al. 2006). Therefore, almost all of the emission from the AGN will be sampled by the SDSS aperture. As the physical radius subtended by the SDSS aperture increases with redshift, a growing fraction of an average galaxy is sampled by the SDSS spectrum. While, at low redshifts, AGN-dominated systems may still have considerable star-formation outside the region probed by the SDSS aperture, at higher redshifts, as more of the galaxy falls within the aperture, AGN-dominated systems become increasingly special objects, containing either fairly luminous AGNs, galaxies with weak SF or objects where most of the SF is either obscured or lies on the outskirts of the galaxy.

Consider an AGN host galaxy with a certain nuclear luminosity L_{AGN} and total SFR. In general, this SFR is spread over the host galaxy, with a fraction f_{in} that lies within the SDSS fiber aperture. The emission line contribution purely from HII regions in the SDSS spectrum is broadly set by SFR and f_{in} (we marginalize over other factors such as host metallicity and morphology for this heuristic argument). If $L_{AGN} > L_{AGN,c}$, a certain critical value, the emission line spectrum of the AGN-ionized gas will be brighter than that from HII regions and the galaxy will enter the AGN-dominated region of the BPT diagram and satisfy our selection. $L_{AGN,c}$ is proportional to the SFR and f_{in} – as $f_{in} \times \text{SFR}$ increases, $L_{AGN,c}$ also increases. Therefore, among strongly SF galaxies or galaxies at higher redshifts (where the SDSS fiber covers a larger part of the host galaxy), AGNs have to be more luminous to enter the AGN-dominated part of the BPT diagram, leaving a larger fraction of the active population in the composite region of the diagram. This effect will also force a correlation between L_{AGN} and SFR among line-selected AGNs, even if one is not physically present.

2.2. WISE All-Sky Survey

The Wide-field Infrared Survey Explorer (WISE Wright et al. 2010) has mapped the entire sky in four MIR bands at 3.4 μm , 4.6 μm , 12 μm and 22 μm . A public catalog is available consisting of photometry from the all-sky survey atlas of point-like and extended sources detected with a $S/N > 5$ in at least one of the four WISE bands. The catalog is not uniform, since the depth of the WISE imaging varies considerably across the sky. The astrometry accuracy of the catalog, tied to the 2MASS coordinate system, is better than 200 mas.

We crossmatched the SDSS-selected AGN with the WISE all-sky survey catalog available from the IPAC/IRSA service, using a simple cone search with a tolerance of 2". More than 98% had a counterpart in the WISE survey, almost 75% of which also had $S/N > 2$ detections in both 12 and 22 μm bands.

We rely on the photometry performed by the WISE all-sky survey pipeline, details of which may be found in

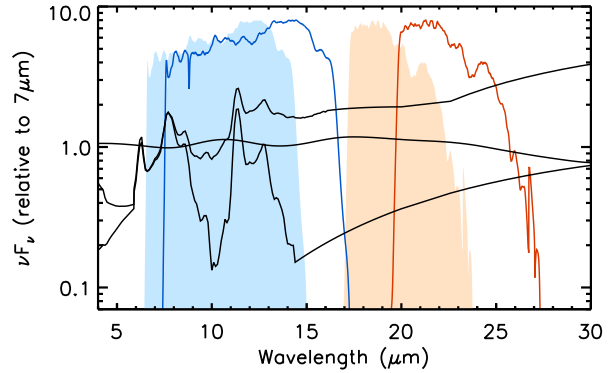


FIG. 1.— An illustration of the WISE W3 and W4 bands and the features of star-forming galaxy and AGN SEDs that are sampled by these bands. Three rest-frame SEDs are shown, all normalized to unity at 7 μm . The two SEDs which show PAH features are SF templates from the Chary & Elbaz (2001) library. The SED with the higher PAH EW corresponds to a total IR luminosity of $10^{10} L_{\odot}$, while that with the lower PAH EW has a total IR luminosity of $10^{12} L_{\odot}$. The relatively featureless AGN SED is the mean template from (Mor & Netzer 2012). The filter functions in the W3 and W4 WISE bands are shown as blue and red curves respectively. The open curves correspond to $z = 0$, while the filled curves show the wavelengths sampled by the filters at $z = 0.15$, the upper redshift limit of the sample studied in this work.

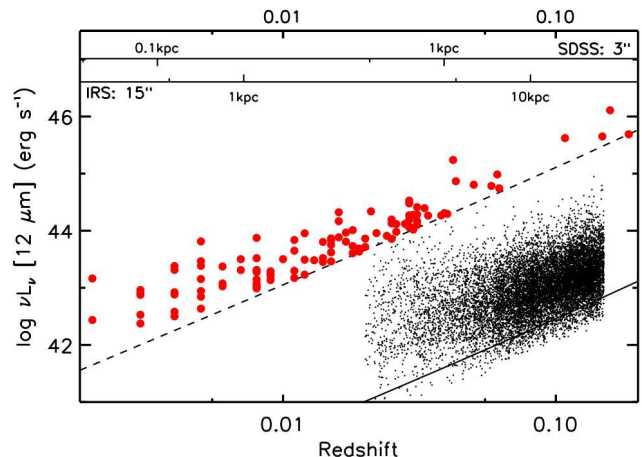


FIG. 2.— Observed-frame 12 μm luminosity vs. redshift of SDSS emission-line selected AGNs (small black points) and Seyferts from the IRAS extended 12 μm sample with Spitzer/IRS spectra from Wu et al. (2009) (large red points). The dashed line shows the limit set by the 0.22 Jy cut used to select the extended 12 μm sample. The solid line shows a nominal limit in the W3 band from the WISE all-sky survey: the actual depth of the survey varies across the sky leading to scatter below the line. Scale bars at the top mark the projected physical radii in kpc spanned by an example circularized IRS aperture size of 15" and the SDSS fiber aperture of 3" diameter.

the Data Release Supplement. The pipeline provides several different photometric measurements for sources in all four WISE bands. The primary photometry is performed by PSF decomposition, assuming that pipeline targets are composed of blends of 1–2 point sources (the ‘profile-fitting’ or PRO photometry). A maximum-likelihood model of the source plane is simultaneously fit in all four bands for contiguous batches of sources. In addition, various flavors of circular and elliptical aperture photometry are also provided by the survey pipeline.

In this work, we only employ photometry in the two

longer wavelength bands. The FWHM of the WISE PSFs are $\approx 6''.8$ in the $12\ \mu\text{m}$ (W3) band and $\approx 11''.8$ in the $22\ \mu\text{m}$ (W4) band. At the lowest redshifts, galaxies could be extended in the WISE images, even beyond the large $22\ \mu\text{m}$ PSF. The profile-fit χ^2 in a band serves as a way to identify if the image of a source in that band is likely to be extended. The WISE pipeline uses a value of reduced $\chi^2 > 3$ to flag a source as extended. We find that, of the roughly 12440 sources in our ‘working sample’ (those with better than 2σ detections in either W3 or W4), only 264 have a reduced $\chi^2 > 3$ in either the W3 or W4 bands: 80% of these lie at $z < 0.05$ and 95% are associated with an extended counterpart in the 2MASS all-sky near-IR survey. The vast majority of the sources in our sample are unresolved in the W3 and W4 bands of WISE and for these we adopt the PRO magnitudes as the best estimates of their photometry. For the resolved sources with 2MASS counterparts, the WISE pipeline generates aperture photometry in ellipses matched and scaled to the sizes and shapes of the corresponding 2MASS sources, which we adopt as the best estimates of their magnitudes. The W3 magnitudes of extended sources have been boosted by a small additive factor of 0.44 mag to account for imperfect background subtraction and other effects shown to influence the aperture photometry (see WISE All-Sky Survey Explanatory Supplement Sec VI.3.e). We exclude the remaining 32 extended sources with no 2MASS counterparts from our sample.

2.2.1. MIR features probed by the WISE bands

In Figure 1, we examine the parts of the IR SEDs sampled by the two WISE bands in both SF and pure AGN torus-dominated cases. Two representative SF galaxy templates from the Chary & Elbaz (2001) library are plotted, corresponding to total IR (8–1000 μm) luminosities of $10^{10}\ L_{\odot}$ (a moderately SF galaxy) and $10^{12}\ L_{\odot}$ (a local Ultra-luminous IR galaxy [ULIRG]). For an torus-dominated SED, we show the template of Mor & Netzer (2012), an average from MIR observations of local Type I AGNs spanning a wide range in luminosity.

At all redshifts in this study, the W3 band covers the complex of emission bands at 8–13 μm produced by Polycyclic Aromatic Hydrocarbons (PAHs) as well as the broad silicate absorption feature at 10 μm . The W4 band, on the other hand, is free of PAHs and serves as a good measure of the pure dust continuum emission, which, in star-forming galaxies, comes from warm dust in the high temperature tail of the typical distribution of grains. Due to the systematic variation of PAH equivalent widths (EWs) with total IR luminosity (Chary & Elbaz 2001; Dale et al. 2001), the W3-W4 colors of SF galaxies are bluer in low luminosity IR galaxies (i.e., those with low levels of SF) than in IR luminous systems, such as ULIRGs.

Compared to SF templates, pure AGN templates are flat and fairly featureless in the 10 – 30 μm wavelength band (Netzer et al. 2007; Mullaney et al. 2011; Mor & Netzer 2012). Theoretical studies of AGN-heated dust ‘tori’ suggest a broad range of peak wavelengths around 15–30 μm depending on the structure of the dust and the intrinsic AGN spectrum (Hönig et al. 2006; Fritz et al. 2006; Nenkova et al. 2008). Real AGNs, how-

ever, frequently show PAH features in their spectra, from SF in their host galaxies. Significant silicate absorption is also found in their SEDs, especially among Type IIs (e.g. Deo et al. 2007; Goulding et al. 2012). The W3-W4 color of a typical AGN lies within the range shown by SF galaxies - a simple color criterion involving these bands cannot easily distinguish between star-formation and AGN dominated systems.

2.2.2. Comparison to IRAS extended 12 μm AGN sample

In Figure 2, we plot observed-frame 12 μm luminosities against redshift of SDSS AGNs with WISE W3 band photometry (small black points) along with a subset of AGNs from the IRAS-based extended 12 μm sample of galaxies (large red points). The latter come from the compilation of Wu et al. (2009) and constitute a large fraction of local Seyferts that have been studied spectroscopically with the Spitzer/IRS instrument (Buchanan et al. 2006; Wu et al. 2009; Tommasin et al. 2010; LaMassa et al. 2010). The selection of the extended 12 μm sample of AGNs was set by the depths of the IRAS Faint Source catalog v2 (Rush et al. 1993) and all have 12 μm fluxes $f_{12,IRAS} \geq 0.22$ Jy. In comparison, the WISE all-sky survey reaches down to 0.5 mJy (2σ) at 12 μm . Therefore, the sources typically studied using detailed IRS spectroscopy are either much nearer or much more luminous than the vast majority of the sources in our sample. From Figure 2, we see that the typical redshift of AGNs from the 12 μm sample is $z \sim 0.02$, whereas most of our AGNs lie at $z \sim 0.1$. Since the scales covered by nominal IRS apertures ($\approx 15''$) are similar to those covered by the WISE PSF, most earlier spectroscopic studies probed AGN hosts on radii of \lesssim few kpc – just the circum-nuclear regions – while most of our AGNs are photometered over the entire galaxy. In addition, our objects cover a much larger swathe of MIR luminosity than existing samples over the redshifts where the two samples overlap, and are not restricted to the IR-luminous systems detected by IRAS. These differences should be borne in mind when comparing our findings to results in the contemporary literature.

2.3. FIRST 20 cm Radio Survey

For a radio survey complementary in many ways to the SDSS, we turn to the VLA-FIRST 20 cm (1.4 GHz) survey (Becker et al. 1995). The current public catalog combines observations of about 10,000 deg^2 of sky coincident with the SDSS. The resolution of the FIRST survey is $\approx 5''$ with an astrometric accuracy of 50 mas. The integrated flux of FIRST sources is measured using two-dimensional gaussian fits to the source profile on the survey maps. For a small fraction of sources which are very extended and jetted, those corresponding to classical radio galaxies, a gaussian profile fit is an inadequate representation of the source structure and the FIRST photometry of such sources may be in error. Since the vast majority of the sources in our sample are at low power ($L_{1.4} < 10^{23}\ \text{W Hz}^{-1}$), the source sizes are likely to be close to or below the resolution of the survey and the fluxes will be accurate.

We crossmatched the SDSS-selected AGN with the FIRST source catalog using a search tolerance of $2''$. This yielded FIRST counterparts for 23% of LINERs and 19%

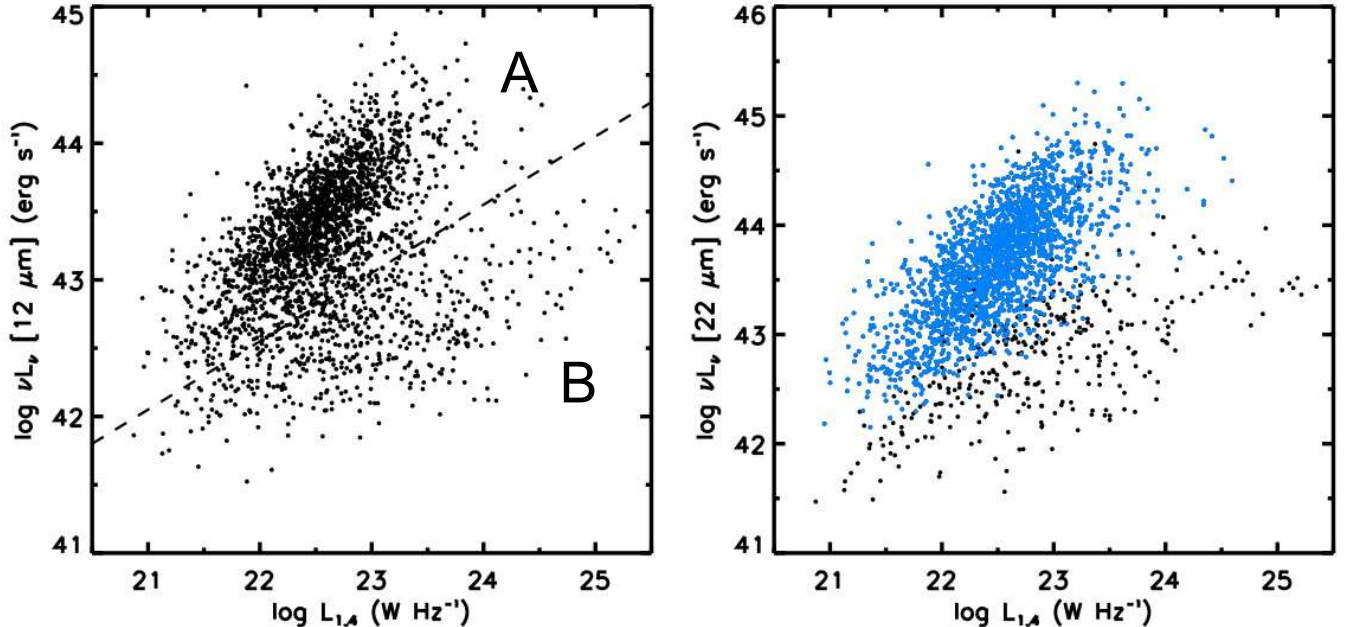


FIG. 3.— **Left:** Rest-frame 12 μm luminosity (L_{12}) vs. 1.4 GHz luminosity ($L_{1.4}$) of SDSS emission-line selected AGNs in the redshift range $0.02 < z < 0.15$. Two populations or “branches” of objects may be discerned which describe different slopes in the correlation between L_{12} and $L_{1.4}$. These have been marked A and B and a dashed line is plotted which roughly divides between the branches. **Right:** Rest-frame 22 μm luminosity (L_{22}) vs. 1.4 GHz luminosity ($L_{1.4}$) of SDSS emission-line selected AGNs in the redshift range $0.02 < z < 0.15$. Based on the division into branches from the left panel, objects are plotted with differently colored points: blue for objects on Branch A and black for objects on Branch B. The division based on L_{12} translates very cleanly into different branches in L_{22} vs. $L_{1.4}$, highlighting the continuity between photometry in the PAH-sensitive W3 band and the continuum-dominated W4 band.

of Seyferts, about $\times 2$ higher than the SDSS counterpart fraction of FIRST sources at the $r < 18$ magnitude limit of the SDSS spectroscopic survey (de Vries et al. 2007). The difference is due to our stringent emission line selection, which picks out more luminous systems. Relaxing the $H\alpha$ EW requirement, for e.g., yields radio detection rates of $\approx 10\%$. Due to the relative shallowness of FIRST, only a subdominant fraction of the AGN population can be probed completely by this study. In the rest of this work, unless otherwise stated, we use the term AGNs, LINERs or Seyferts to refer to the subpopulations detected in both WISE and FIRST surveys.

2.4. AKARI All-Sky survey

The far-infrared (FIR) is dominated by radiation from cold dust with temperatures $< 100\text{K}$. In galaxies, this component of the dust emission spectrum is produced almost exclusively in star-forming regions or from diffuse cirrus. In FIR luminous galaxies, the component from star-formation is paramount and, even in fairly luminous AGNs, the FIR luminosity can be taken as a relatively clean measure of the SFR (e.g. Netzer et al. 2007; Rosario et al. 2012).

In Section 3.2, we investigate the relationship between SF and the MIR luminosity of AGNs. For a sample of bonafide star-forming AGNs to aid in this study, we identify a subset of FIR-bright AGNs from the AKARI/FIS all-sky survey Bright Source Catalog. We crossmatch our AGNs with the catalog using a search tolerance of $15''$. The large tolerance is warranted by the greater positional uncertainty of the FIR catalog due to the broad AKARI PSF at $90 \mu\text{m}$ ($\approx 50''$ FWHM). 703 sources were identified with reliable $90 \mu\text{m}$ photometry ($\text{FQUAL90} = 3$).

The 0.55 Jy detection limit of the AKARI/FIS catalog corresponds to a $90 \mu\text{m}$ luminosity limit of $\approx 10^9 L_{\odot}$ at $z = 0.02$ and $\approx 10^{10.9} L_{\odot}$ at $z = 0.15$, picking out moderately luminous star-forming galaxies at all redshifts.

3. TWO POPULATIONS OF AGNS: THE MIR-RADIO PLANE

In this section, we demonstrate that AGNs divide into two relatively distinct populations in the plane of MIR and radio luminosity. Seyferts and LINERs distinguish themselves by differentiating into these two populations in different proportions. We examine the effects of survey limits and whether this dichotomy is preserved even among radio-undetected AGNs.

The rest-frame monochromatic MIR luminosities at 12 and $22 \mu\text{m}$ used here are derived from the WISE W3 and W4 magnitudes, applying a k-correction based on a Chary & Elbaz (2001) template of a star-forming galaxy with a total IR luminosity of $10^{11} L_{\odot}$. The k-correction is small, amounting to 0.03 mag at $12 \mu\text{m}$ and 0.4 mag at $22 \mu\text{m}$ for galaxies at $z = 0.15$. The full range of IR templates from Chary & Elbaz (2001) gives a maximum variation in the k-correction of ± 0.2 magnitudes. A flat radio spectrum per unit energy was assumed, requiring no additional k-correction to get rest-frame 1.4 GHz luminosities. Since the radio output of a sizable fraction of AGNs is governed by star-formation (Section 5.2.3), true spectra indices may vary as high as 0.5. However, the choice of spectral index makes no significant difference to our results.

In the left panel of Figure 3, we plot the rest-frame $12 \mu\text{m}$ monochromatic luminosity (L_{12}) against the rest-frame 1.4 GHz luminosity ($L_{1.4}$) of SDSS/WISE/FIRST

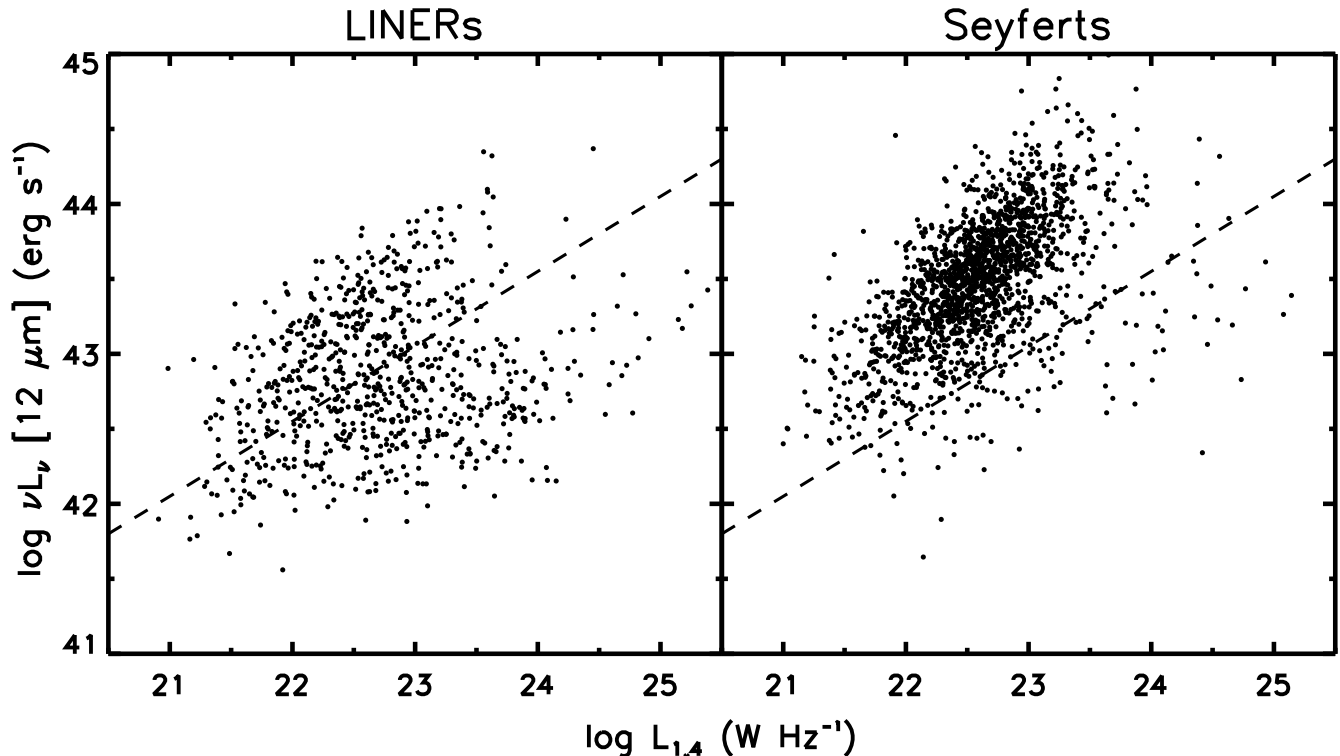


FIG. 4.— Rest-frame 12 μm luminosity (L_{12}) vs. 1.4 GHz luminosity ($L_{1.4}$) of SDSS emission-line selected AGNs in the redshift range $0.02 < z < 0.15$. The dashed line which divides the two branches from Figure 3 is also plotted. LINERs and Seyferts are shown in the left and right panels respectively. The two classes of AGNs distribute very differently in this diagram. While LINERs occupy both branches, Seyferts are almost completely on Branch A.

AGNs. They divide quite clearly into two fairly distinct populations in the L_{12} – $L_{1.4}$ plane. We use the term ‘branches’ to describe the two populations and will refer to them as such in the rest of the paper. Objects on Branch A have a high $L_{12}/L_{1.4}$ ratio and delineate a steep trend between 12 μm luminosity and radio luminosity. On Branch B, sources show a lower $L_{12}/L_{1.4}$ ratio and a shallow dependence between L_{12} and $L_{1.4}$. The dashed line in the Figure roughly separates the two branches and serves as a guide to the eye.

The two branches persist in the plot of L_{22} vs. $L_{1.4}$ (right panel of Figure 3), but the lower branch is less populated. This is because of the shallower depth of the WISE survey in the W4 band: IR faint objects are not significantly detected in W4, which preferentially affects the density of objects in Branch B. Nevertheless, this diagram shares many features in common with the left panel, implying a close continuity between the emission of AGNs in both MIR bands. Indeed, if one divides sources into two branches based on their position in the left panel, they remain in two branches in the right panel as well (as shown with different colored points).

In Figure 4, we show the L_{12} – $L_{1.4}$ plane separately for LINERs and Seyferts. Remarkably, despite being divided purely based on optical emission line criteria, the two AGN classes show strikingly different behavior in this diagram. Seyferts cluster tightly and typically lie at $L_{12} > 10^{43}$ erg s $^{-1}$, almost exclusively along Branch A ($\approx 6\%$ of Seyferts lie on Branch B). On the other hand, LINERs divide roughly equally between both branches. LINERs on Branch A are slightly less luminous in L_{12} than Seyferts of the same $L_{1.4}$, tending to lie closer to

the dividing line.

The division of AGNs into two branches based on MIR and radio properties is preserved across all redshifts in our sample (left panel of Figure 5), though the most luminous sources, both in the MIR and the radio, are found at the higher redshifts simply because of the larger volumes probed. The characteristic flux limits of the WISE and FIRST surveys correspond to an increasing L_{12} and $L_{1.4}$ luminosity limit with redshift (dashed vertical and horizontal lines). Sources on Branch A are luminous enough in the MIR that they lie well above the luminosity limit at all redshifts. The normalization and slope of Branch A in the L_{12} – $L_{1.4}$ plane does not appear to change with redshift, suggesting a physical basis for this Branch which remains constant to $z = 0.15$. Sources in Branch B typically lie just around the L_{12} limit - this suggests that the weak slope to this Branch is not real, but is driven mostly by Malmquist bias.

As discussed before, the relative shallowness of the FIRST survey ultimately limits the fraction of AGNs that can be classified into branches, ranging from 40% at $z = 0.02$ to 15% at $z = 0.1$. In contrast, the deep WISE photometry allows us to estimate MIR luminosities for most SDSS AGNs, since more than 90% of the parent sample are detected in the W3 band. Could the L_{12} distribution of sources undetected in FIRST give us an indication as to their likely location on the MIR–Radio plane? Is the coherence of Branch A seen at low redshifts preserved among AGNs at high redshifts that lie below the FIRST flux limits?

To overcome the complexities of redshift-dependent limits, we consider a narrow redshift slice at $0.080 <$

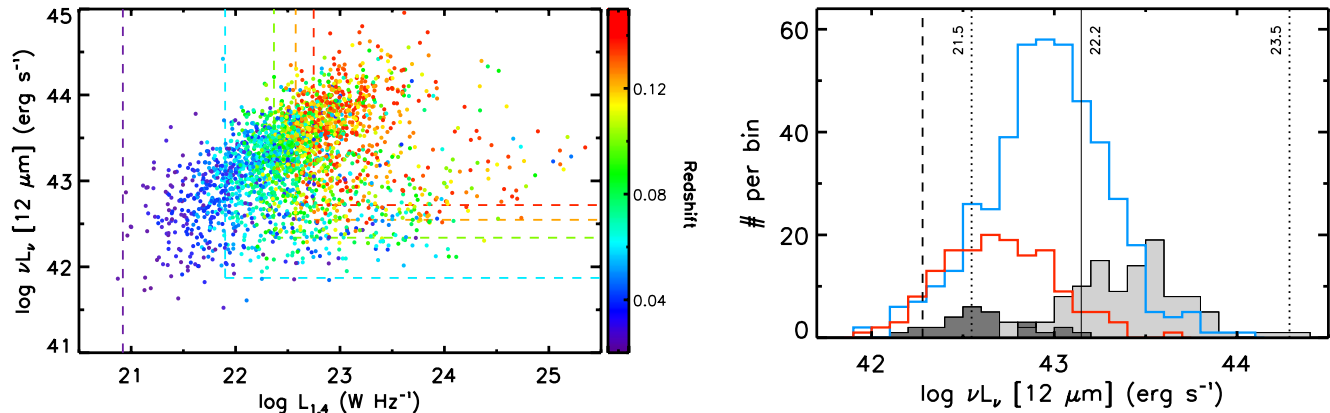


FIG. 5.— **Left:** Rest-frame $12 \mu\text{m}$ luminosity (L_{12}) vs. 1.4 GHz luminosity ($L_{1,4}$) of SDSS emission-line selected AGNs colored by redshift, according to the colorbar at right. The dashed lines show the typical luminosity limit of the WISE and FIRST surveys at a set of illustrative redshifts, also colored according to the same colorbar. Sources on Branch A are considerably brighter than the L_{12} limits at their corresponding redshifts and the correlation on the diagram from objects on this Branch is seen consistently at all redshifts. On the other hand, sources on Branch B lie close to the L_{12} limits at all redshifts. The weak correlation seen for Branch B is driven mostly by redshift biases, in that the most luminous sources are seen only at the highest redshifts in our sample. **Right:** L_{12} distributions of AGNs in the narrow redshift interval $0.080 < z < 0.085$. The dashed vertical line shows the typical L_{12} limit probed by the WISE survey at these redshifts. Three vertical lines mark the L_{12} values of the ridgeline of Branch A at $\log L_{1,4} = 21.5$ (left dotted), 22.2 (solid) and 23.5 (right dotted) W Hz^{-1} , spanning the range of radio luminosity covered by Branch A over the entire AGN sample. The shaded histograms show sources that are detected in the FIRST survey. Sources on Branch A (light gray histogram) and Branch B (dark gray histogram) show different distributions of L_{12} , as expected from their locations on the MIR-Radio plane. The colored open histograms show sources that lie below the FIRST detection limit. The L_{12} distribution of radio-undetected Seyferts (blue histogram) is consistent with most of them lying on an extrapolation of Branch A below the FIRST detection limit. The L_{12} distribution of radio-undetected LINERs (red histogram) is consistent with a substantial fraction on Branch B, in parallel with radio-detected LINERs.

$z < 0.085$, roughly at the middle of the full range of redshifts. In the right panel of Figure 5, we compare the L_{12} distributions of the radio-detected and -undetected SDSS/WISE AGNs and attempt to understand their differences. One may view these histograms as a projection of the MIR-Radio plane of Figure 3 onto the Y-axis for sources in the small redshift interval. For the 17% of the sources detected in FIRST, we plot distributions of L_{12} split by Branch, as shown by the grey histograms. The L_{12} of FIRST-detected sources is bimodal, consistent with the patterns in the MIR-Radio plane. Of the remaining sources, those detected in the W3 band but undetected by FIRST comprise 77% of the full SDSS sample at these redshifts. These are plotted as the open colored histograms in the Figure, with Seyferts shown in blue and LINERs shown in red. Our hypothesis is that a substantial fraction of LINERs should be on an extension of Branch B below the radio limit, while Seyferts should mostly lie on Branch A. Their L_{12} distributions should reflect this and this is indeed what we observe.

FIRST-undetected LINERs show an L_{12} distribution that clusters close to the MIR limit (dashed line) and has a similar shape to that of FIRST-detected objects on Branch B, though with a tail to more luminous sources. This is very consistent with the observed distribution of radio-detected LINERs: a substantial fraction of objects on Branch B, with a small number on Branch A leading to the luminous tail. In contrast, the radio-undetected Seyferts show a distribution peaking roughly between the histograms of the two branches. Most Seyferts have L_{12} much higher than the MIR luminosity limit, consistent with them lying on an extension of Branch A below the radio limit.

We can illustrate this more quantitatively in the following manner. Since the ridgeline of Branch A has

a non-zero slope in the MIR-Radio plane, sources with higher $L_{1,4}$ correspond to higher L_{12} , with some scatter given by the width of Branch A. For a representative set of $L_{1,4}$ above, at and below the FIRST detection limit at $z = 0.08$, we calculate corresponding L_{12} from the Branch A ridgeline (see Figure 6) and plot them as vertical solid and dotted lines. The range of L_{12} spanned by the dotted lines is equivalent to the range spanned by the entirety of Branch A galaxies over our entire redshift range. It encompasses the Branch A histogram at this redshift (by construction) as well as the peak of the Seyferts. The solid line, corresponding to the radio detection limit, delineates a transition between the radio-detected sources of Branch A and the peak of the radio-undetected Seyferts, as one would expect if a substantial fraction of these Seyferts lay on an extension of Branch A.

4. THE NATURE OF THE TWO BRANCHES

Here we investigate the likely cause for the splitting of the AGN into two populations in MIR-Radio space. This has important implications for our understanding of the AGN population. If the dichotomy is driven by differences in the level of SF-heated dust, then our results would imply that the vast majority of Seyferts are in SF galaxies, even those with AGN-dominated nuclear emission lines. If, on the other hand, the difference is driven by a higher level of AGN-heated dust in Seyferts, then the MIR-Radio diagram may be viewed as a sensitive tracer of reprocessed high energy radiation from AGN and will allow us some insight into the intrinsic differences in the nuclear SEDs of these two classes of systems. Our approach is to devise a series of empirical tests which make use of the high-quality ancillary data and measurements available for SDSS galaxies.

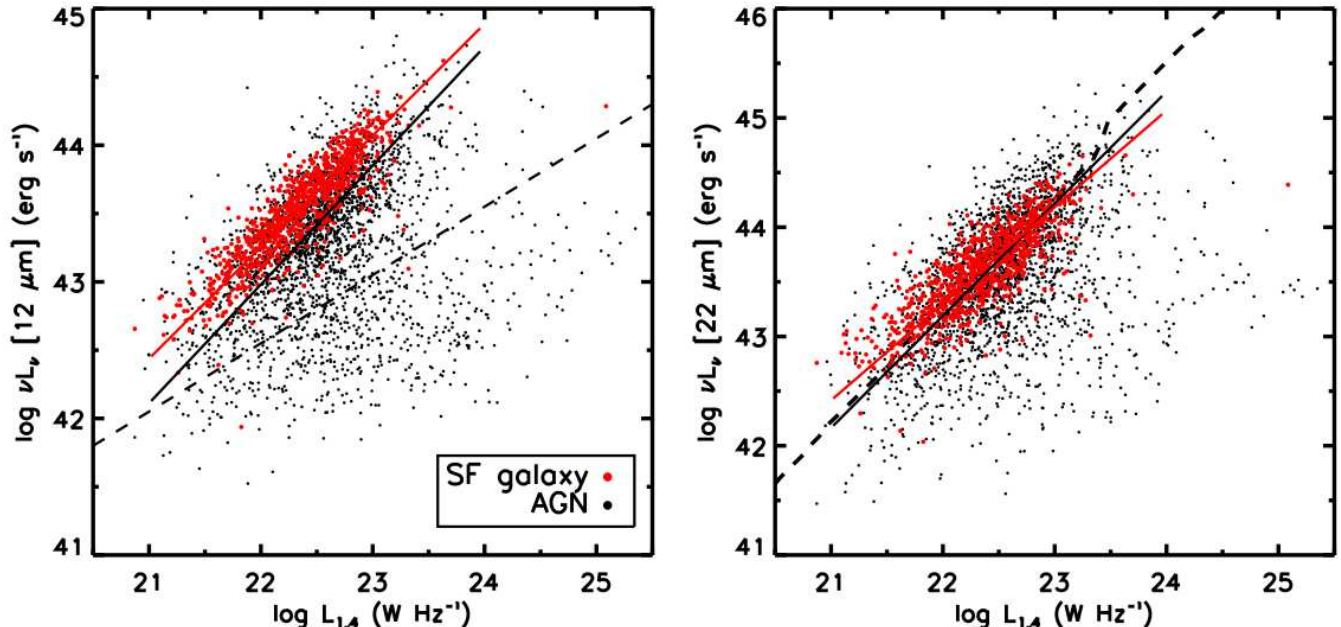


FIG. 6.— **Left:** Rest-frame 12 μm luminosity (L_{12}) vs. 1.4 GHz luminosity ($L_{1.4}$) of SDSS selected AGNs (black points) and a control sample of inactive star-forming galaxies (red points) in the redshift range $0.02 < z < 0.15$. The dashed line is the same as in Figure 3. Also shown are regression lines from fits to the inactive star-forming galaxies (red line) and AGNs on Branch A (black line) that are matched to inactive galaxies. The L_{12} - $L_{1.4}$ trend for SF galaxies is offset from that of the AGNs on Branch A. **Right:** Rest-frame 22 μm luminosity (L_{22}) vs. 1.4 GHz luminosity ($L_{1.4}$) of SDSS selected AGNs (black points) and a control sample of inactive star-forming galaxies (red points) in the redshift range $0.02 < z < 0.15$. Also shown are regression lines from fits to the inactive star-forming galaxies (red line) and AGNs on Branch A (black line) that are matched to inactive galaxies. The thick dashed line shows the FIR-radio correlation of SF galaxies from Sargent et al. (2010), extrapolated to 22 μm using SF templates from Chary & Elbaz (2001). Both SF galaxies and AGNs on Branch A lie along this correlation, and scatter consistently about it.

4.1. Star-Forming galaxies on the MIR-Radio plane

A simple empirical diagnostic is the location of pure inactive, star-forming galaxies in MIR-Radio space. AGNs are mostly found in fairly massive galaxies ($M_* \gtrsim 10^{10.5} M_\odot$) and, since many galaxy properties, including SFR, correlate strongly with stellar mass, a fair comparison of SF properties between AGNs and inactive galaxies requires, minimally, that the comparison take into account stellar mass related biases (Silverman et al. 2009; Xue et al. 2010; Rosario et al. 2013). For this, we construct a control sample of pure star-forming galaxies matched to AGN in both redshift and M_* . We select galaxies which lie below the curve that separates star-forming from composite systems in the BPT diagram (Eqn. 1 in Kewley et al. 2006). To ensure good discrimination in this diagram, we also require the galaxies to be detected with a $S/N > 3$ in the $H\alpha$, $H\beta$ and $[\text{N II}]\lambda 6584$ emission lines. Only a valid upper limit is needed on $[\text{O III}]\lambda 5007$ to select SF galaxies in this manner. After binning the AGNs and inactive galaxies in $\Delta \log M_* = 0.1$ bins in stellar mass and $\Delta z = 0.01$ bins in redshift, we randomly assign one inactive galaxy to each AGN in a bin. In practice, since there exist very few purely SF galaxies with large stellar masses, some AGNs are left unmatched at the high mass end ($M_* \gtrsim 10^{11.5} M_\odot$). We account for the unmatched AGNs in the following analysis. The inactive control sample was crossmatched to the WISE All-sky survey catalog and the VLA-FIRST catalog in the same fashion as the AGNs, and the MIR and radio photometry were extracted from these catalogs in a similar way.

In Figure 6, we plot again the MIR-Radio diagrams for the AGN, as in Figure 3, but also include the SF galaxies as red points. The SF galaxies describe a tight relation in MIR-Radio space. In the L_{12} - $L_{1.4}$ diagram (left panel), the SF galaxies overlap with the upper end of the distribution of AGNs on Branch A, but essentially no inactive SF galaxies are found on Branch B. SF galaxies also lie exclusively on Branch A in the L_{22} - $L_{1.4}$ diagram (right panel), but here the SF galaxies generally overlap with the AGNs. In both panels, linear regression lines for AGNs and inactive galaxies are shown, estimated using an ordinary-least-squares (OLS) bisector algorithm. Only the AGNs from Branch A that were successfully matched to inactive galaxies are used in the regression analysis. The relative trends for both sets of objects can be compared at a glance.

In the right panel of Figure 6, we include as well the ridge line of the FIR-radio correlation found among SF galaxies (e.g. Condon 1992; Sargent et al. 2010), extrapolated to rest-frame 22 μm using the SF templates of Chary & Elbaz (2001). The increased contribution of warm dust in the MIR at the transition between normal SF galaxies and luminous IR galaxies (LIRGs), as modelled by Chary & Elbaz (2001), is responsible for the kink in the shape of this line in this diagram; real galaxy populations likely show a smoother relationship. Inactive SF galaxies and AGNs on Branch A scatter quite symmetrically about the FIR-radio correlation, implying that the 22 μm luminosity of both is largely produced by SF heated dust.

A closer look at the ratio of MIR-to-radio luminosity

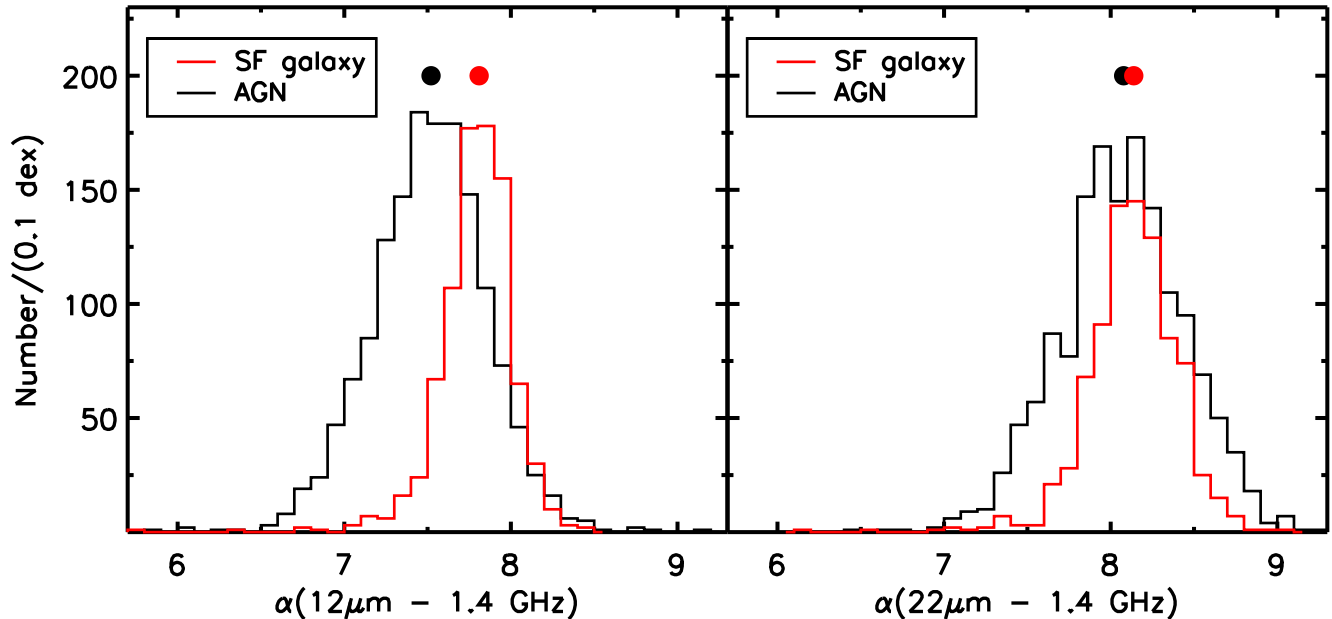


FIG. 7.— Distributions of the rest-frame MIR-Radio spectral index α , the ratio of the $12\ \mu\text{m}$ luminosity (left panel) or $22\ \mu\text{m}$ luminosity (right panel) to the $1.4\ \text{GHz}$ luminosity. The distributions of α for AGNs on Branch A (black histograms) may be compared to those of mass-matched SF galaxies (red histograms). The median values of each distribution are marked with appropriate red or black circular points at the top of each panel.

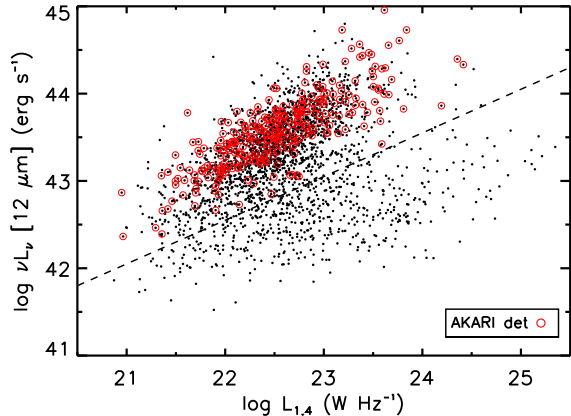


FIG. 8.— Rest-frame $12\ \mu\text{m}$ luminosity (L_{12}) vs. $1.4\ \text{GHz}$ luminosity ($L_{1.4}$) of SDSS selected AGNs (black points) in the redshift range $0.02 < z < 0.15$. Sources detected at $90\ \mu\text{m}$ in the AKARI/FIS all-sky survey are marked with open red circles. Every one of these FIR-bright SF host galaxies lies on Branch A.

brings out the differences at $12\ \mu\text{m}$ and $22\ \mu\text{m}$. We define a MIR-Radio spectral index $\alpha = L_\nu[\text{MIR}]/L_\nu[1.4\ \text{GHz}]$, where the MIR= 12 or $22\ \mu\text{m}$. In Figure 7, we compare the α distributions of stellar mass-matched SF inactive galaxies and AGNs on Branch A. The SF galaxies always show a narrower distribution than the AGNs. While the median α values for both sets of objects are approximately the same at $22\ \mu\text{m}$, differing by 0.06 dex, the AGNs are weaker compared to the SF galaxies at $12\ \mu\text{m}$ by 0.29 dex. We discuss possible reasons for these differences in Section 5. Since L_{22} is more consistent with an origin in SF, we use only $22\ \mu\text{m}$ measurements in further tests.

As a final test of the relationship between Branch A

and star-formation, we plot the location of the AKARI $90\ \mu\text{m}$ detected sources on the L_{12} - $L_{1.4}$ diagram for AGNs (Figure 8). Given the depth of the AKARI/FIS survey, the hosts of these AGNs must be forming stars at a modest rate of several to tens of M_\odot/yr . Every single AKARI detected source lies on Branch A, which strongly reinforces the conclusion that this Branch marks the location of SF host galaxies in the MIR-Radio plane.

4.2. The relation between D_n4000 and MIR luminosity

The optical spectral index D_n4000 , sensitive to the strength of the 4000\AA break, is a good measure of the light-weighted specific SFR (sSFR) of galaxies (Brinchmann et al. 2004). If the two branches identified above do indeed correspond to AGNs with different levels of on-going SF in their hosts, one may expect a difference in the D_n4000 distributions of AGNs in the two branches. This is tested in Figure 9, where we plot D_n4000 against L_{22}/M_* . If the $22\ \mu\text{m}$ luminosity is determined primarily by the SFR of the AGN hosts, then L_{22}/M_* will be proportional to the sSFR and, therefore, tracked by D_n4000 . Indeed, we find a strong anticorrelation between D_n4000 and L_{22}/M_* . In addition, objects from the two branches are reasonably well separated in this diagram. Branch B AGNs have a higher D_n4000 , clustering around a value of 1.9 at which the sensitivity of D_n4000 as a tracer of stellar age saturates in old stellar populations. In contrast, objects in Branch A show typically much smaller D_n4000 , peaking around a value of 1.4 and form much of the ridgeline of the correlation in the Figure. Clearly, the separation of AGNs into two branches also largely separates them by sSFR.

In addition to the AGNs, we also plot the modal trend between D_n4000 and sSFR from Brinchmann et al. (2004) as a green line in the Figure. We have used

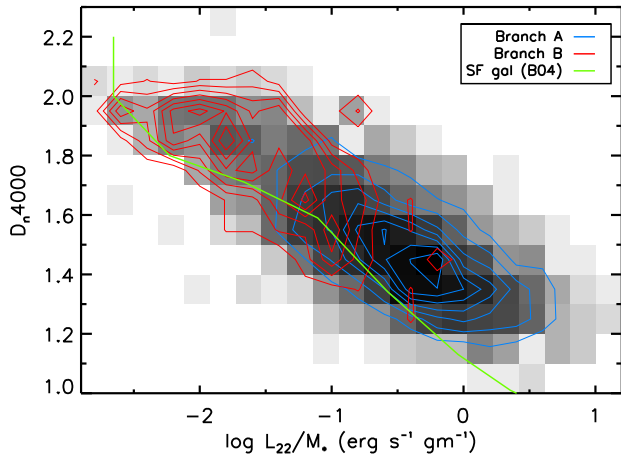


FIG. 9.— D_n4000 vs. the ratio of L_{22} to stellar mass (M_*) of SDSS selected AGNs in the redshift range $0.02 < z < 0.15$ plotted as a density map. A \sinh^{-1} stretch is applied to the map to enhance low density regions. A strong anticorrelation is seen, as expected if L_{22} is related to SFR. There is a marked difference in the location of objects from Branch A (blue contours) and Branch B (red contours) on this plot. The green solid line shows the ridgeline (modal trend) of the correlation between D_n4000 and sSFR from Brinchmann et al. (2004), adapted to this Figure using a relation between SFR and L_{22} derived from the calibration of Kennicutt (1998) and the SED library of Chary & Elbaz (2001).

the SED library of Chary & Elbaz (2001), along with the relation between SFR and L_{FIR} from Kennicutt (1998), to convert between SFR and L_{22} and place the Brinchmann et al. (2004) line on this Figure. At a given L_{22}/M_* , AGNs have a higher D_n4000 than those of SF galaxies, irrespective of the Branch to which they belong. We have checked that galaxies from our SF inactive control sample lie along the Brinchmann et al. (2004) line, verifying that the offset we see for AGNs is not due to systematic differences in the estimation of the SFR from L_{22} (Brinchmann et al. (2004) calibrate SFRs from $H\alpha$). Since we have shown that the L_{22} of AGNs and SF galaxies are not systematically different, certainly not at the level of ≈ 0.3 dex needed to reconcile the AGNs and SF trends in Figure 9, this would suggest that AGNs have higher D_n4000 than SF galaxies of similar stellar mass, or, alternatively, AGNs show a lower sSFR than SF galaxies. At face value, this is puzzling, given the similarity in the galaxy integrated sSFRs of the two populations as traced by their $22 \mu\text{m}$ luminosity distributions. However, the difference makes more sense if we recall the aperture-related selection effects of SDSS spectroscopic samples. BPT-selection of AGN-dominated systems systematically selects *against* objects with strong SF in the SDSS fiber aperture, while the selection of pure SF galaxies selects *for* strong central SF. Against the backdrop of the older bulge stellar populations found in massive galaxies, this selection effect will naturally lead to lower measured sSFRs for the AGNs.

4.3. Radio-loudness and its relation to the Branches

Further examination of Figure 3 reveals an interesting connection between the strength of radio emission and the division into branches. Consider the small number of sources with $L_{1.4} > 10^{24} \text{ W Hz}^{-1}$, which are too radio-loud to be powered by even the most luminous SF galaxies. We find that most of these sources lie on Branch

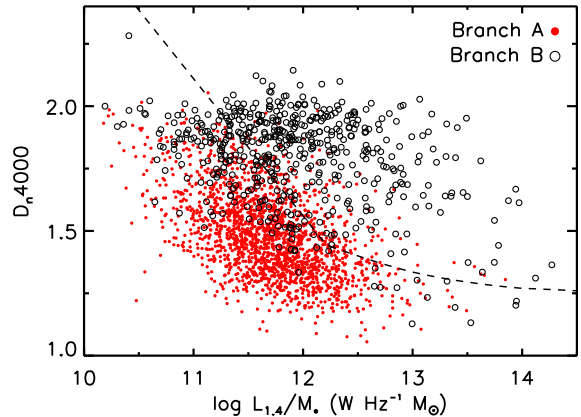


FIG. 10.— D_n4000 vs. the ratio of $L_{1.4}$ to stellar mass (M_*) of SDSS selected AGNs in the redshift range $0.02 < z < 0.15$. The dashed line is from Best & Heckman (2012); radio-loud sources lie above the line in this diagram. There is a marked difference in the location of objects from Branch A (red filled points) and Branch B (black open circles). The radio-loud region of the diagram is occupied mostly by objects on Branch B.

B, with relatively few radio galaxies lying on Branch A. We can explore this connection more robustly by plotting D_n4000 against the specific radio luminosity ($L_{1.4}/M_*$) of our AGNs (Figure 10). This plot was first proposed in Best et al. (2005) and recalibrated in Best & Heckman (2012) as a way to identify sources with a strong radio excess over that produced by SF. Pure star-forming galaxies with a range of SF histories lie along a fixed locus in this diagram and below the dashed line in Figure 10. Above the line, sources may be treated as radio-loud.

As one may see at a glance, sources on Branch A lie primarily in the radio-quiet, SF-dominated part of the diagram, with only 12% lying above the dashed line. Sources on Branch B straddle the line, but most are in the radio-loud part of the diagram. As hinted by Figure 3, radio-loud AGNs in our sample lie mostly on Branch B. The scatter about the separation line depends on a complex set of factors such as the biases of BPT AGN selection (Section 2.1.1) and SDSS aperture effects, since $L_{1.4}$ tracks the galaxy integrated radio luminosity, while D_n4000 only traces the inner stellar populations. However, we take the broad separation of the branches in this diagram as evidence that radio-loud AGNs lie preferentially on Branch B, while Branch A is preferentially populated by radio-quiet SF hosts.

The dearth of SF signatures and MIR weakness in powerful radio galaxies (with $L_{1.4} > 10^{26} \text{ W Hz}^{-1}$) is well-known from previous studies (e.g. Ogle et al. 2006; Shi et al. 2007; Dicken et al. 2012). Comparisons of radio-loud quasars and radio galaxies also indicate high MIR optical depths in the latter (Leipski et al. 2010) and boosted non-thermal emission in the former (Cleary et al. 2007), both of which must be considered in a complete picture of the relative MIR-to-radio properties of radio-loud systems.

4.4. AGN-heated dust in the MIR

Till now, our tests have connected star-formation and the emission of AGN hosts in the long-wavelength MIR. However, given the expected prominence of AGN-heated dust at these wavelengths, it is important as well to con-

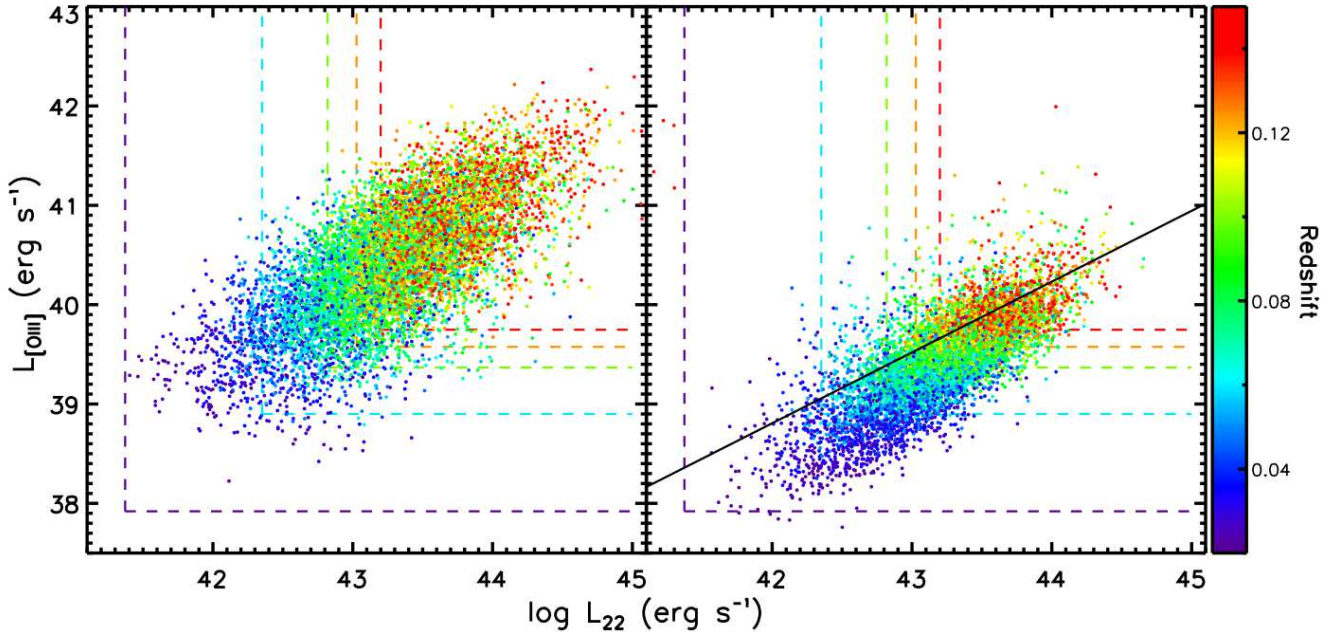


FIG. 11.— [O III] λ 5007 luminosity ($L_{[OIII]}$) vs. rest-frame $22\ \mu\text{m}$ luminosity (L_{22}) of SDSS emission-line selected AGNs (left panel) and pure SF galaxies (right panel) colored by redshift, according to the colorbar at right. The dashed lines show the typical luminosity limit of the WISE and SDSS spectroscopic surveys at a set of illustrative redshifts, also colored according to the same colorbar. Both sets of galaxies show a correlation between $L_{[OIII]}$ and L_{22} . For a given L_{22} , SF galaxies have much lower $L_{[OIII]}$ and tend to cluster close to the SDSS luminosity limits at all redshifts. The solid black line in the right panel is an envelope that contains below it 80% of all SF galaxies in this diagram.

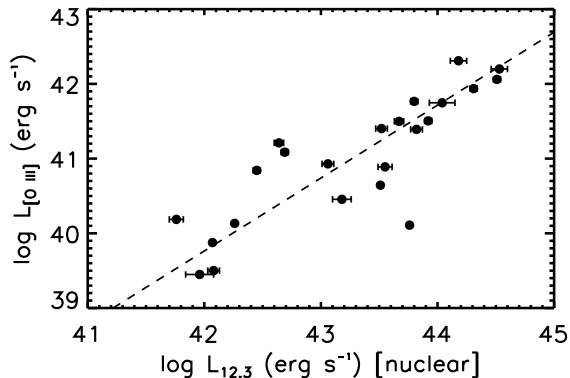


FIG. 12.— The correlation between the nuclear $12.3\ \mu\text{m}$ luminosity (measured within $1''$) and the integrated [O III] λ 5007 luminosity from the Narrow-Line Region of a set of nearby AGNs. The dashed line is a OLS bisector fit to the data points. See Section 4.3 for details.

strain the contribution from the AGN.

4.4.1. The L_{22} - $L_{[OIII]}$ relation in AGNs and star-forming galaxies

A simple test for the influence of the AGN in the MIR is shown in the left panels of Figure 11, where we plot L_{22} against $L_{[OIII]}$ for all WISE-detected AGNs, including those that are not detected in the FIRST survey. In AGN-dominated galaxies, the [O III] emission lines are a good measure of the intrinsic luminosity of the AGN, since they originate in the highly ionized Narrow Line Region (NLR). In this and following plots, we only use the observed [O III] λ 5007 luminosities without applying

any correction for NLR dust extinction. This is because the accuracy of an extinction correction from the $H\alpha/H\beta$ Balmer decrement, is highly dependent on the flux uncertainties of the $H\alpha$ and $H\beta$ emission lines. This will lead to inaccurate corrections for objects with fainter emission line fluxes, such as low luminosity and distant AGNs. Therefore, and also for consistency with the compilation of [O III] luminosities discussed below, we present our analyses using uncorrected $L_{[OIII]}$. However, we have tested our results using a fixed extinction of $A_V = 0.8$ the typical value estimated for the brighter AGNs in our sample. The basic conclusions remain unchanged.

We find that AGNs show a good correlation between $L_{[OIII]}$ and L_{22} . The correlation suggests either that the AGN contributes significantly to the luminosity of host galaxies at $22\ \mu\text{m}$, or, alternatively, that the total SF in AGN-dominated galaxies tracks nuclear activity. Similar results have been shown before for AGN-dominated galaxies from the SDSS using other tracers of the SFR, such as D_n4000 (Netzer 2009). We discuss these alternatives in more detail in Section 5.3.

Note that purely SF galaxies from our control sample also show a strong correlation between $L_{[OIII]}$ and L_{22} , as demonstrated in the right panel of Figure 11. The slope of this correlation is similar to that shown by AGNs, but it is shifted towards lower $L_{[OIII]}$ by 1.7 dex. Given the characteristic flux limits of the SDSS spectra, which are translated to luminosity limits at different redshifts and plotted as dashed lines in the Figure, one concludes that, the correlation seen in SF galaxies is mostly shaped by Malmquist bias. At progressively higher redshifts, only galaxies luminous at both $22\ \mu\text{m}$ and in [O III] will be selected, tightening the correlation. Nevertheless, we can

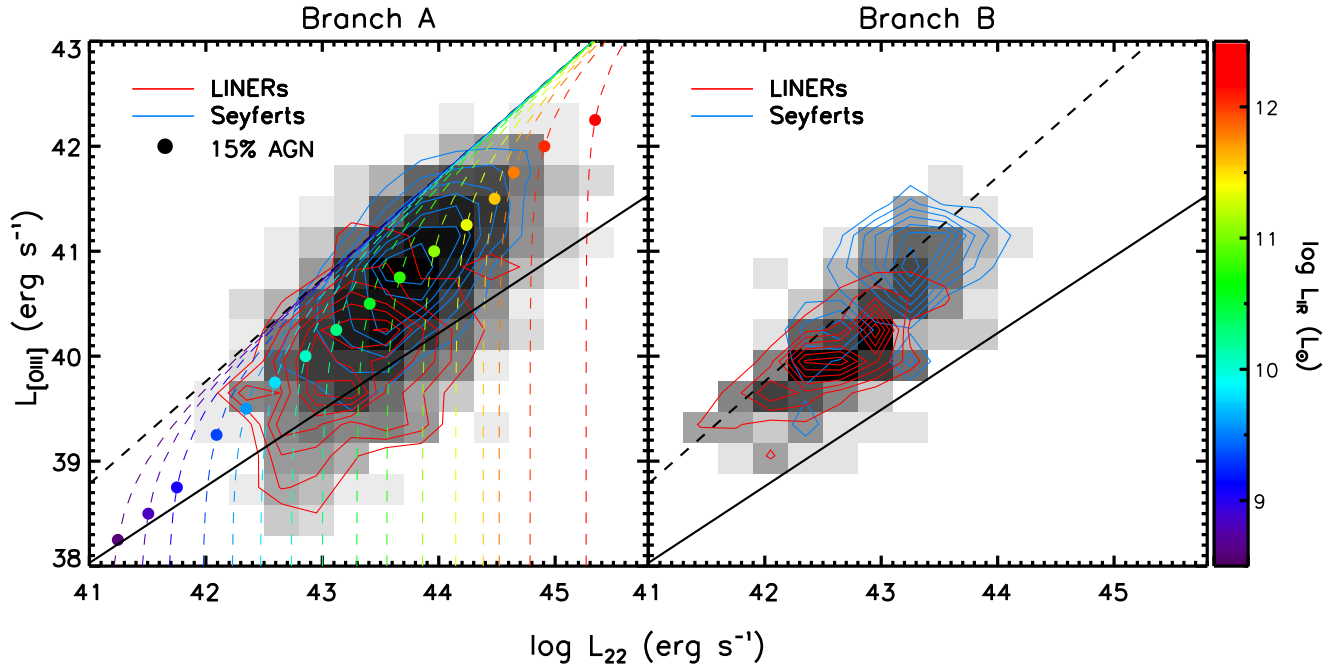


FIG. 13.— $[\text{O III}]\lambda 5007$ luminosity ($L_{[\text{OIII}]}$) vs. rest-frame $22\ \mu\text{m}$ luminosity (L_{22}) of SDSS emission-line selected AGNs on Branch A (left panel) and Branch B (right panel), plotted as a density map. A \sinh^{-1} stretch is applied to the map to enhance low density regions. In each panel, the locations of Seyferts (blue contours) and LINERs (red contours) are also shown. The solid black line is the 80% envelope of SF galaxies (see Figure 11), while the dashed black line shows the location of a pure AGN template on this diagram. The colored dashed lines in the left panel show the loci of hybrid templates of star-forming galaxies containing AGN, with a SF-powered IR luminosity indicated by the colorbar at right. As the AGN luminosity traced by $L_{[\text{OIII}]}$ reaches a level where it starts to dominate the MIR luminosity of a hybrid template, the loci transition from a fixed L_{22} to a sloped line on which AGN-dominated systems lie. The colored filled circles mark the location on the hybrid template loci where the AGN accounts for 15% of L_{22} . Since the MIR in AGNs on Branch B is not governed by star-formation, hybrid templates are not plotted in the right panel.

use our sample to constrain the degree to which emission from SF may contribute to the $[\text{O III}]\lambda 5007$ emission in the AGNs. We construct an envelope which contains 80% of SF galaxies, shown as a solid line in the Figure, which we compare below to the location of the AGNs on this diagram.

4.4.2. The intrinsic MIR luminosity of AGNs

Before we can embark on this exercise, we require a predictor for the intrinsic MIR luminosity of the AGN which we can compare to the measured MIR luminosity of the WISE-detected sources. Many studies have used MIR spectroscopy to empirically investigate the relation between nuclear power and the MIR continuum or PAH luminosity in nearby and distant AGNs (e.g. Lutz et al. 2004; Shi et al. 2007; Diamond-Stanic & Rieke 2010; LaMassa et al. 2010). Most studies rely on fairly large apertures in the MIR – for e.g., with the Spitzer IRS spectrograph, the workhorse for most of such studies, typical apertures used to extract spectra correspond to scales of a few to several kpc. The contribution of SF-heated dust to the long-wavelength MIR in such spectra could be substantial. Therefore, we turn to a high resolution (sub-arcsec) photometric study of the MIR emission in local AGNs using narrow-band imaging from the VISIR instrument on the VLT (Gandhi et al. 2009; Asmus et al. 2011). These small-scale observations greatly limit host galaxy dilution and isolate, as best as currently possible, the AGN-heated torus emission from the nucleus. Having said this, in some cases the VISIR measurements may still have a substantial SF contribution from starbursts

on tens of pc scales (Asmus et al. 2011).

For a set of $[\text{O III}]\lambda 5007$ emission line fluxes, we employ the compilation of Whittle (1992), which uses a coherent methodology to account for aperture losses, bringing consistency to the varied nature of spectroscopic studies of AGNs in the Local Universe. Whittle (1992) only provide observed line fluxes, uncorrected for extinction, but since we use uncorrected $L_{[\text{OIII}]}$ in our full analysis, we directly adopt these measurements. Combining $12.3\ \mu\text{m}$ luminosities with $L_{[\text{OIII}]}$ for Seyferts in common to the two datasets, we establish a tight correlation between these quantities (Figure 12) which we fit using an OLS bisector regression algorithm. The correlation is tighter for the more luminous AGNs, but the scatter increases at lower luminosities, possibly due to a higher level of SF contamination among such systems. Nevertheless, we use our best-fit relationship to estimate a $12.3\ \mu\text{m}$ luminosity for an AGN given $L_{[\text{OIII}]}$:

$$L_{12.3} = 1.02L_{[\text{OIII}]} + 1.24 \quad (1)$$

Armed with this relationship, we construct a set of hybrid IR templates of AGNs embedded in star-forming hosts. The average MIR template of Type I AGNs from Mor & Netzer (2012) is combined with the SF SED library of Chary & Elbaz (2001), scaling the AGN template using Equation 1 to cover a range of nominal AGN luminosities in the range $L_{[\text{OIII}]} = 10^{38-43}\ \text{erg s}^{-1}$. The resulting set of hybrid templates span a wide range in MIR AGN dominance, from sub-percentile to 100% AGN emission at $22\ \mu\text{m}$. There is considerable scatter of both

real galaxy and AGN SEDs about our adopted templates, so these models are not exact for any individual object, but will serve as a guide to the typical behavior of star-forming AGN hosts with varying degrees of nuclear emission.

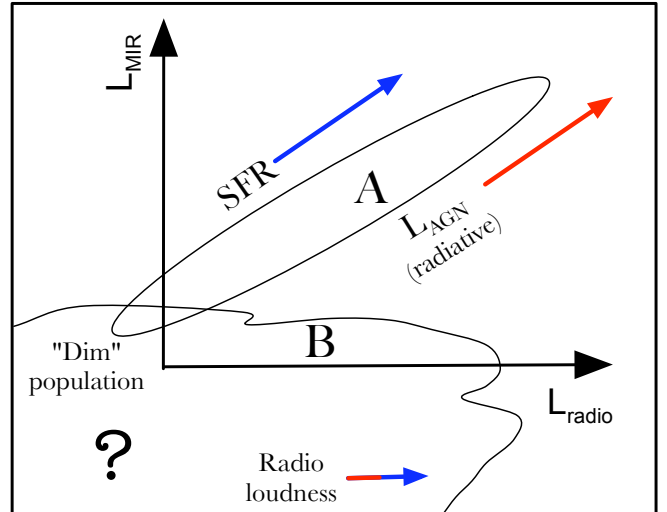
4.4.3. The star-formation/AGN mixing diagram

In Figure 13, we again plot $L_{[OIII]}$ against L_{22} , now only for sources with both FIRST and WISE detections, i.e., the subsample which can be classified into branches. The distribution of AGNs are shown as a density map, but now splitting the AGNs by panel into the two branches. Overplotted on the left panel over the distribution for Branch A is the loci of the hybrid templates, shown as dashed lines colored by SF-powered IR luminosity. These lines are not plotted on the right panel since the MIR luminosity of the objects in Branch B probably does not arise from recent star-formation.

The hybrid template loci have a characteristic shape: as the AGN luminosity in a particular hybrid increases, it moves along a track of increasing $L_{[OIII]}$ at a fixed L_{22} till the AGN fraction at $22\ \mu\text{m}$ starts to approach unity. At this point, all loci bend onto the pure AGN line (dashed line in both panels). Naturally, the characteristic AGN $L_{[OIII]}$ at the turnover is a function of the IR luminosity of the SF template. Interestingly, among the luminous IR galaxies (with $L_{IR} > 10^{11}\ \text{erg s}^{-1}$), it is possible to conceal the MIR emission of quite a luminous AGN, with $L_{[OIII]}$ as high as $10^{41}\ \text{erg s}^{-1}$ ($L_{bol} \approx 4 \times 10^{44}\ \text{erg s}^{-1}$, based on the bolometric correction of Heckman et al. 2004).

A key point to take from Figure 13 is that the L_{22} of pure AGN templates is quite close to the observed L_{22} for the AGNs, given their $[OIII]$ luminosities. Disentangling SF and nuclear components of the MIR luminosity in these AGNs is therefore not trivial. Nevertheless, we proceed given our assumptions about the intrinsic AGN luminosity and the SEDs of AGNs and SF components, and discuss some of the complexities in Section 5.

AGNs from both branches show a correlation between L_{22} and $L_{[OIII]}$. In detail, there are some differences between the behavior of the two branches in the diagram. The characteristic $L_{[OIII]}$ of AGNs in Branch B is lower than that for Branch A, a consequence primarily of the larger fraction of low-luminosity LINERs in Branch B. The ridgeline of the Branch B distribution lies closer to the pure AGN locus than that of Branch A, as can be judged from the sequence of large colored circular points plotted in the left panel of the diagram. The points show the location on the template loci where the AGN accounts for 15% of L_{22} , chosen to run through the peak of the Branch A distribution. Clearly the sources on Branch B are more AGN dominated in the MIR, even though they contain less luminous AGNs. Having said this, we see that the ridgeline of the Branch B distribution is still slightly offset from the pure AGN locus, most clearly for the LINERs. This could reflect the presence of additional sources of weak MIR emission such as cirrus heating by evolved stars (Sauvage & Thuan 1992; Calzetti et al. 1995; Groves et al. 2012) or the synchrotron tail from relativistic particles (e.g. Yuan 2007) which only become prominent in low-luminosity systems with minimal SF and AGN heating.



Scenario 1

Scenario 2

FIG. 14.— Schematic descriptions of the two scenarios for the origin of the branches in the MIR-radio plane outlined in Section 5. The two branches are labelled ‘A’ and ‘B’ as from Figure 3. The “dim” population which lie below the joint WISE and FIRST detection limits, is designated with a question mark signifying our lack of knowledge of their true MIR-radio relationship. Scenario 1, denoted in blue, assumes that star-formation purely governs the location of AGN hosts on Branch A. Scenario 2, denoted in red, assumes that pure AGN emission governs all patterns on the MIR-radio plane. See Section 5.2 for more details and a discussion.

In both panels of Figure 13, we use different colored contours to show the location of Seyferts and LINERs in each panel. As expected, Seyferts have higher $L_{[OIII]}$ than LINERs in both branches. In fact, some LINERs on Branch A are weak enough in $[OIII]$ to place them in the region occupied by the star-forming galaxies. A substantial fraction of the line emission in such systems could arise from HII regions. In addition to this, the LINERs on Branch A show a weaker correlation between $L_{[OIII]}$ and L_{22} than the Seyferts on the same Branch. Their typical location on the diagram is also further away from the AGN line than the Seyferts, indicating that such star-forming LINERs are even more dominated at $22\ \mu\text{m}$ by SF-heated dust.

It is worth noting that the median $L_{[OIII]}$ of LINERs on Branch A and Branch B are similar despite an order of magnitude difference in their median L_{22} . This also highlights the conclusion that the separation of the AGN population into branches is mostly governed by processes unrelated to their direct nuclear emission.

5. DISCUSSION

5.1. Summary of empirical results

The patterns exhibited by AGNs in Figures 3 and 4 strongly suggest the existence of distinct populations (branches) of active galaxies, differentiated by their MIR-to-radio properties. Intimately connected to the nature of the branches is the origin of the integrated (i.e., galaxy-wide) MIR emission of the AGNs. Before proceeding with an interpretive discussion, we summarize what we have learned about the branches from the various tests performed above.

Sources on **Branch A**: have higher absolute MIR luminosities than those on Branch B (Figure 3); describe a

steep trend in MIR-radio space, shared with SF galaxies (Figure 6); account for 95% of Seyfert AGNs and 50% of LINERs (Figure 4); are consistent with the median MIR-radio relationship of SF galaxies at $22\ \mu\text{m}$ (Figure 7); are offset low from the median MIR-radio relationship of SF galaxies at $12\ \mu\text{m}$ by ≈ 0.3 dex (Figure 7); have a larger scatter in their MIR-radio distribution compared to SF galaxies (Figure 7); include all FIR-bright AGN hosts with substantial SF (Figure 8); have a low median $D_n4000 \approx 1.4$ (Figure 9); are largely radio-quiet, with radio luminosities consistent with a SF origin (Figure 10); are consistent with typically low AGN contributions at $22\ \mu\text{m}$ of 15% (Figure 13).

In comparison, sources on **Branch B**: have lower absolute MIR luminosities than those on Branch A (Figure 3); describe a shallow trend in MIR-radio space, consistent with uncorrelated scatter modulated by redshift-dependent MIR luminosity limits (Figure 5); account for 50% of LINERs and only 5% of Seyferts (Figure 4); lie well off the MIR-radio relationship of SF galaxies (Figure 6); have a higher $D_n4000 = [1.6, 2.0]$ (Figure 9); account for most radio-loud AGNs (Figure 10); are more AGN-dominated in the MIR than Branch A (Figure 13).

5.2. Origin of the Branches in the MIR-Radio plane

Our investigation has revealed evidence for a mixture of different heating mechanisms for dust in the hosts of AGNs: star-formation, nuclear light and possibly a contribution from cirrus heated by the UV background in galaxies. Here we critically examine the role of these mechanisms in the nature of the branches. First we consider two simplified alternate explanations, which allow us to conceptually explore the assumptions and conclusions one may draw from the empirical analyses of the last two sections. Then we consider the consequences of combining these alternatives towards a more realistic and nuanced picture of the MIR properties of AGNs.

We begin by outlining two extreme and opposite positions: 1) The $12\text{--}22\ \mu\text{m}$ luminosity of AGNs on Branch A is dominated by SF-heated dust, or, 2) The $12\text{--}22\ \mu\text{m}$ luminosity of AGNs on both branches are dominated by AGN-heated dust. These scenarios are outlined schematically on the MIR-radio plane in Figure 14. In both cases, we assume there is a substantial population of non star-forming, low-luminosity AGN hosts most of which lie below the joint SDSS, WISE and FIRST detection limits. We term this the “dim” population, signifying their weakness in both SF and nuclear emission. We do not speculate here on the MIR-radio relationship of the dim population, representing them instead as a cloud with a question mark signifying our lack of knowledge. Only a small fraction, the tip of the iceberg, are detected in our sample, perhaps due to higher than average levels of dust in their hosts heated by the AGN or the diffuse UV field, or possibly shocks from radio jets. These constitute the systems on Branch B. Fully detected AGNs lie within the quadrant delineated by the axes in Figure 14.

5.2.1. Star-Formation as the origin of the Branches

This scenario is represented using blue arrows and lines in Figure 14. In addition to the dim population described above, there is a set of AGNs found in galaxies with widespread star-formation. These galaxies will have elevated

IR and radio luminosities over the dim population and lie along the correlation between IR and radio continuum luminosities. They constitute Branch A.

Support for this scenario comes from the various relationships between the nature of the branches and measures of SF. Objects on Branch A show a tight correlation between L_{22} and D_n4000 , while most Branch B AGNs lie in evolved systems (Section 4.2). FIR-bright AGNs all lie on Branch A (Section 4.1). But the most crucial constraint comes from the correspondence between the $L_{22}\text{--}L_{1.4}$ relationship of Branch A and that of pure SF galaxies. This correlation is widely understood to be set by the close relationship between the non-thermal output from supernovae and the UV emission from young stars, reprocessed to the IR. If AGN-heated dust significantly affected L_{22} , we would have seen an offset towards higher $22\ \mu\text{m}$ luminosities among the AGNs, which we do not observe, except perhaps among some of the brightest AGNs in our sample. This, as well as the constraints from hybrid templates and the radio-loudness test, suggests that the MIR luminosity, as well as the radio luminosity, of most AGNs on Branch A is dominated by SF.

Interestingly, the $12\ \mu\text{m}$ luminosity of AGNs on Branch A is too low at a given $L_{1.4}$ to be fully consistent with SF galaxies. In other words, AGNs on Branch A have redder W3-W4 colors than SF galaxies of the same (radio-based) SFR. Two effects may account for this. One is the suppression of PAH excitation or the destruction of PAH grains in AGN-dominated systems, as suggested by recent Spitzer/IRS spectroscopic studies of large samples of SDSS AGNs (LaMassa et al. 2012). Additionally, strong $10\ \mu\text{m}$ Si absorption troughs, frequent in Type II AGNs (Shi et al. 2006; Hao et al. 2007), could contribute to the offset.

5.2.2. AGN emission as the origin of the Branches

In Figure 14, red arrows and lines represent the scenario where the hot-dust emission from the AGN torus ultimately sets the patterns in the MIR-Radio plane. For this to be the case, our estimate of the intrinsic MIR AGN luminosity would have to be systematically in error, to account for the ~ 0.7 dex in L_{22} needed to reconcile the ridgeline of the AGN trend with the AGN-dominated line in Figure 13. This estimate is based on high resolution $12\ \mu\text{m}$ photometry of very nearby AGNs combined with the best current knowledge of their intrinsic MIR SEDs. It may be that the low to moderate luminosity AGNs in our sample have a redder mean MIR SED than existing studies currently suggest, leading to a more luminous $22\ \mu\text{m}$ luminosity than we apply to our hybrid templates. This is supported by studies of the typical SEDs of low luminosity AGNs (e.g. Ho 2008), though at the higher AGN luminosities among our sample, the Mor & Netzer (2012) SED should be accurate.

In this scenario, the two branches represent a bimodal distribution of AGNs with different levels of radio output relative to their thermal (accretion disk) output. This is akin to the well-known “Radio-loud/Radio-quiet” dichotomy (e.g. Sikora et al. 2007). Objects on Branch B are low luminosity AGNs that span a range in radio luminosity and may be fueled by so-called “hot-mode” accretion, while objects on Branch A, which contain most luminous AGNs and Seyferts, have a more defi-

nite relationship between their thermal and non-thermal output and are fueled mostly by “cold-mode” accretion (Best & Heckman 2012).

An AGN-dominated MIR SED may help explain the redder W3-W4 color of AGN hosts compared to SF galaxies, since pure AGN SED templates, such as that of Mor & Netzer (2012), which lack PAH emission bands, are usually redder than the templates of weakly SF galaxies. Having said this, SF-related features, such as low ionization emission lines and PAH bands are known to be fairly common in the MIR spectra of AGN hosts (e.g. Weedman et al. 2005; Buchanan et al. 2006; Wu et al. 2009), so pure AGN-dominated MIR SEDs in all systems does not have much empirical support. Earlier studies have reported a higher average AGN contribution to the MIR than we find (e.g., $> 45\%$ among Type II AGN at $19 \mu\text{m}$ in Tommasin et al. 2010), but this is almost certainly because most existing spectroscopic samples target rather nearby systems and sample only the inner few kpc of the host galaxy (Figure 2), missing most of the continuum and PAH luminosity emitted by SF on larger galactic scales.

Besides this, an AGN-dominated scenario would still have to explain the close relationships found between the branches and SF indicators, as well as the conspiracy that the $L_{22}\text{--}L_{1.4}$ of the AGNs on Branch A, set only by the intrinsic AGN output in this picture, overlaps that of pure SF galaxies. The processes that govern the relative non-thermal output in AGNs (e.g., the Poynting flux from the magnetosphere of an SMBH) is drastically different from those that set the non-thermal output of SF regions (i.e., shock acceleration in supernova remnants), so a common slope and normalization for the trends in the MIR-Radio plane is very unlikely.

5.2.3. A mixed origin

In our analysis of the $L_{[OIII]}\text{--}L_{22}$ diagram, we show that both SF and AGN-heated emission are expected to produce luminosities close to the values seen among real AGNs. This suggests that the MIR luminosity of AGNs, especially those on Branch A, is likely a mixture of AGN-heated and SF-heated components. The investigation using hybrid templates suggests that the component from SF probably dominates by a small margin, accounting for, on average, $\sim 85\%$ of L_{22} . However, the AGN-heated component sets a floor to the MIR luminosity – even if the SFR of an AGN host galaxy is low, its total MIR luminosity cannot drop below the level set by the nuclear component.

A mixed origin for Branch A could contribute to the broader width of the $\alpha(22 \mu\text{m}\text{--}1.4 \text{ GHz})$ distribution for AGNs on this Branch (Figure 7). The SFR of the host galaxy places a particular AGN at a particular location on the locus of SF galaxies in the MIR-Radio plane. AGN activity can potentially boost both the MIR and radio luminosity over the level set by the SFR. If the AGN is radio-weak but IR bright, it will scatter the system above the Branch A ridgeline. Alternatively, if the AGN is relatively radio-bright, it will scatter the system below the ridgeline by increasing its $L_{1.4}$ without changing its MIR luminosity significantly. Differing combinations of radio and MIR luminosity will scatter objects off the SF locus, leading to the broader distribution we see among AGNs. The slight asymmetry in the shape of the $\alpha(22$

$\mu\text{m}\text{--}1.4 \text{ GHz})$ distribution may indicate that the scatter from enhanced radio emission is larger than the scatter from AGN MIR emission. However, further careful study are necessary to test this notion.

5.3. The Star-Forming Properties of AGNs

One of the most interesting results from our study is that 95% of SDSS/WISE/FIRST Seyfert galaxies lie on Branch A, while lower luminosity LINERs are more frequently on Branch B. We have shown that most objects on Branch A have considerable on-going SF. This implies a relationship between the ionization of AGN emission lines and star formation in their hosts.

The characteristic low $L_{[OIII]}$ of LINERs imply that they are low-luminosity AGNs. Studies have shown that they are typically in massive, evolved hosts with low levels of SF (e.g. Ho 2008; but see Tommasin et al. 2012). An examination of Panel 1 in Figure 4 suggests that a fraction of LINERs have on-going SF, though their typical SFRs, as tracked by their MIR luminosity on Branch A, are lower than in Seyferts. Combined with the fact that a large fraction of LINERs lie on Branch B, our results add support to the view that LINERs are found mostly in quiescent or quenching hosts.

On the other hand, the very high fraction of Seyferts on Branch A is evidence that most Seyferts are in actively star-forming host galaxies. This is consistent with GALEX-based UV studies that show that so-called “bright AGNs” in the SDSS are found among fairly normal SF galaxies (Salim et al. 2007). Since the ionization state of AGNs is strongly correlated with $L_{[OIII]}$, such bright emission-line selected AGNs are essentially all Seyferts. Bright AGNs are known to have lower D_n4000 than lower-luminosity AGNs, indicative of younger mean stellar ages (Kauffmann et al. 2003b). Morphological studies also reveal that Seyfert hosts are generally in massive galaxies with disks and active SF, while early-type galaxies hosting bright AGNs frequently show anomalously blue colors suggestive of on-going SF (e.g. Schawinski et al. 2010). Studies of X-ray selected AGNs from deep extragalactic survey fields also show a high frequency of SF host galaxies, compared to similarly massive inactive galaxies (Silverman et al. 2009; Rosario et al. 2013). This suggests that radiatively efficient nuclear activity, which powers X-ray and emission-line bright AGNs, is associated with on-going SF in the host galaxy. This can be explained by many diverse models, such as connected nuclear starbursts and AGN fueling (Davies et al. 2007), merger-induced AGN activity (Hernquist 1989), accretion from stellar mass loss (Ciotti & Ostriker 2007), or their combinations. Alternatively, since both efficient nuclear fueling and SF rely on the same supply of material, namely cold gas, the connection seen here may be simply governed by the stochastic availability of this fuel, rather than any real causal link between the AGN and galaxy-wide SF (e.g. Rosario et al. 2013).

The correlation between $L_{[OIII]}$ and L_{22} for objects on Branch A (left panel of Figure 13) also seems to suggest a correlation between the global SFR of AGNs and their nuclear luminosity. However, as described in Section 2.1.1, an important selection effect inherent to AGN-dominated systems selected on the BPT diagram, can play a role in strengthening this correlation, if not driv-

ing it completely. Thus, we may expect to see a relationship between $L_{[OIII]}$ and L_{22} even if a strong correlation does not physically exist. Obviously a more complete assessment of correlations between the SFR and AGN activity will require the inclusion of composite systems that host AGNs, which entails other measures of AGN luminosity or a careful treatment of their spectra in order to separate AGN and SF contributions to the emission line luminosity. This will be undertaken in future work.

6. CONCLUSIONS

We investigate the trends between the radio and long-wavelength MIR luminosities of narrow-line (Type II) emission-line selected AGNs from the SDSS, which reveals characteristic patterns in the MIR-Radio plane, suggestive of two distinct populations or “branches”. Building on the substantial ancillary data from the SDSS, as well as AKARI FIR photometry, we devise various tests to help unveil the properties of the two branches. Objects on Branch A are generally radio-quiet, have younger central stellar populations and exhibit an IR-radio relationship consistent with that of normal inactive SF galaxies, though with suppressed luminosity at $12\ \mu\text{m}$. Objects on Branch B account for most radio-loud AGN, have evolved central stellar populations and lie well off the location of SF galaxies on the MIR-Radio plane, implying that their MIR emission is unrelated to SF. These tests demonstrate that the galaxy-integrated MIR luminosity of AGNs on Branch A arises primar-

ily from dust heated by on-going SF. A correlation between the $[O\ III]\lambda 5007$ luminosity and the MIR luminosity suggests a possible relationship between SF and nuclear emission, but important selection effects inherent to emission-line selected AGNs may also account for some or all of the trend. We highlight the result that the majority of Seyfert galaxies lie on (or are consistent with lying on) Branch A, which suggests a connection between the processes that govern SF and the fueling of radiatively-efficient AGN activity. The MIR-Radio plane is a useful tool in studies of the SF and accretion properties of AGNs over a range of nuclear luminosities.

We thank Hagai Netzer and Li Shao for useful discussions. Funding for the SDSS and SDSS-II has been provided by the Alfred P. Sloan Foundation, the Participating Institutions, the National Science Foundation, the U.S. Department of Energy, the National Aeronautics and Space Administration, the Japanese Monbukagakusho, the Max Planck Society, and the Higher Education Funding Council for England. The SDSS Web Site is <http://www.sdss.org/>. This publication makes use of data products from the Wide-field Infrared Survey Explorer, which is a joint project of the University of California, Los Angeles, and the Jet Propulsion Laboratory/California Institute of Technology, funded by the National Aeronautics and Space Administration. This research also employs observations with AKARI, a JAXA project with the participation of ESA.

REFERENCES

- Abazajian, K. N., Adelman-McCarthy, J. K., Agüeros, M. A., et al. 2009, *ApJS*, 182, 543
- Asmus, D., Gandhi, P., Smette, A., Hönig, S. F., & Duschl, W. J. 2011, *A&A*, 536, A36
- Baldwin, J. A., Phillips, M. M., & Terlevich, R. 1981, *PASP*, 93, 5
- Becker, R. H., White, R. L., & Helfand, D. J. 1995, *ApJ*, 450, 559
- Bennert, N., Jungwiert, B., Komossa, S., Haas, M., & Chini, R. 2006, *A&A*, 456, 953
- Best, P. N., & Heckman, T. M. 2012, *MNRAS*, 421, 1569
- Best, P. N., Kauffmann, G., Heckman, T. M., & Ivezić, Ž. 2005, *MNRAS*, 362, 9
- Brinchmann, J., Charlot, S., White, S. D. M., et al. 2004, *MNRAS*, 351, 1151
- Buchanan, C. L., Gallimore, J. F., O’Dea, C. P., et al. 2006, *AJ*, 132, 401
- Calzetti, D., Bohlin, R. C., Kinney, A. L., Storchi-Bergmann, T., & Heckman, T. M. 1995, *ApJ*, 443, 136
- Calzetti, D., Kennicutt, R. C., Engelbracht, C. W., et al. 2007, *ApJ*, 666, 870
- Chary, R., & Elbaz, D. 2001, *ApJ*, 556, 562
- Churazov, E., Sazonov, S., Sunyaev, R., et al. 2005, *MNRAS*, 363, L91
- Cid Fernandes, R., Stasińska, G., Mateus, A., & Vale Asari, N. 2011, *MNRAS*, 413, 1687
- Ciotti, L., & Ostriker, J. P. 2007, *ApJ*, 665, 1038
- Clavel, J., Schulz, B., Altieri, B., et al. 2000, *A&A*, 357, 839
- Cleary, K., Lawrence, C. R., Marshall, J. A., Hao, L., & Meier, D. 2007, *ApJ*, 660, 117
- Condon, J. J. 1992, *ARA&A*, 30, 575
- Dale, D. A., Helou, G., Contursi, A., Silbermann, N. A., & Kolhatkar, S. 2001, *ApJ*, 549, 215
- Davies, R. I., Müller Sánchez, F., Genzel, R., et al. 2007, *ApJ*, 671, 1388
- de Vries, W. H., Hodge, J. A., Becker, R. H., White, R. L., & Helfand, D. J. 2007, *AJ*, 134, 457
- Deo, R. P., Crenshaw, D. M., Kraemer, S. B., et al. 2007, *ApJ*, 671, 124
- Desert, F.-X., Boulanger, F., & Puget, J. L. 1990, *A&A*, 237, 215
- Diamond-Stanic, A. M., & Rieke, G. H. 2010, *ApJ*, 724, 140
- . 2012, *ApJ*, 746, 168
- Dicken, D., Tadhunter, C., Axon, D., et al. 2012, *ApJ*, 745, 172
- Draine, B. T., & Li, A. 2001, *ApJ*, 551, 807
- . 2007, *ApJ*, 657, 810
- Fritz, J., Franceschini, A., & Hatziminaoglou, E. 2006, *MNRAS*, 366, 767
- Gandhi, P., Horst, H., Smette, A., et al. 2009, *A&A*, 502, 457
- Genzel, R., & Cesarsky, C. J. 2000, *ARA&A*, 38, 761
- Genzel, R., Lutz, D., Sturm, E., et al. 1998, *ApJ*, 498, 579
- Goulding, A. D., Alexander, D. M., Bauer, F. E., et al. 2012, *ApJ*, 755, 5
- Groves, B., Krause, O., Sandstrom, K., et al. 2012, *MNRAS*, 426, 892
- Hao, L., Weedman, D. W., Spoon, H. W. W., et al. 2007, *ApJ*, 655, L77
- Heckman, T. M., Kauffmann, G., Brinchmann, J., et al. 2004, *ApJ*, 613, 109
- Heller, C. H., & Shlosman, I. 1994, *ApJ*, 424, 84
- Hernquist, L. 1989, *Nature*, 340, 687
- Ho, L. C. 2008, *ARA&A*, 46, 475
- Hönig, S. F., Beckert, T., Ohnaka, K., & Weigelt, G. 2006, *A&A*, 452, 459
- Juneau, S., Dickinson, M., Alexander, D. M., & Salim, S. 2011, *ApJ*, 736, 104
- Kauffmann, G., Heckman, T. M., White, S. D. M., et al. 2003a, *MNRAS*, 341, 33
- Kauffmann, G., Heckman, T. M., Tremonti, C., et al. 2003b, *MNRAS*, 346, 1055
- Kennicutt, Jr., R. C. 1998, *ARA&A*, 36, 189
- Kewley, L. J., Dopita, M. A., Sutherland, R. S., Heisler, C. A., & Trevena, J. 2001, *ApJ*, 556, 121
- Kewley, L. J., Groves, B., Kauffmann, G., & Heckman, T. 2006, *MNRAS*, 372, 961
- LaMassa, S. M., Heckman, T. M., Ptak, A., et al. 2010, *ApJ*, 720, 786
- . 2012, *ApJ*, 758, 1
- Leipski, C., Haas, M., Willner, S. P., et al. 2010, *ApJ*, 717, 766

- Lutz, D., Maiolino, R., Spoon, H. W. W., & Moorwood, A. F. M. 2004, *A&A*, 418, 465
- Maccarone, T. J., Gallo, E., & Fender, R. 2003, *MNRAS*, 345, L19
- Meléndez, M., Kraemer, S. B., Schmitt, H. R., et al. 2008, *ApJ*, 689, 95
- Merloni, A., Heinz, S., & di Matteo, T. 2003, *MNRAS*, 345, 1057
- Mor, R., & Netzer, H. 2012, *MNRAS*, 420, 526
- Mullaney, J. R., Alexander, D. M., Goulding, A. D., & Hickox, R. C. 2011, *MNRAS*, 414, 1082
- Nardini, E., Risaliti, G., Salvati, M., et al. 2008, *MNRAS*, 385, L130
- Nenkova, M., Sirocky, M. M., Nikutta, R., Ivezić, Ž., & Elitzur, M. 2008, *ApJ*, 685, 160
- Netzer, H. 2009, *MNRAS*, 399, 1907
- Netzer, H., Lutz, D., Schweitzer, M., et al. 2007, *ApJ*, 666, 806
- Norman, C., & Scoville, N. 1988, *ApJ*, 332, 124
- O'Dowd, M. J., Schiminovich, D., Johnson, B. D., et al. 2009, *ApJ*, 705, 885
- Ogle, P., Whysong, D., & Antonucci, R. 2006, *ApJ*, 647, 161
- Rosario, D. J., Santini, P., Lutz, D., et al. 2012, *A&A*, 545, A45
- . 2013, *ApJ*, 771, 63
- Rowan-Robinson, M., & Crawford, J. 1989, *MNRAS*, 238, 523
- Rush, B., Malkan, M. A., & Spinoglio, L. 1993, *ApJS*, 89, 1
- Salim, S., Rich, R. M., Charlot, S., et al. 2007, *ApJS*, 173, 267
- Sanders, D. B., Phinney, E. S., Neugebauer, G., Soifer, B. T., & Matthews, K. 1989, *ApJ*, 347, 29
- Sanders, D. B., Soifer, B. T., Elias, J. H., et al. 1988, *ApJ*, 325, 74
- Sargent, M. T., Schinnerer, E., Murphy, E., et al. 2010, *ApJS*, 186, 341
- Sauvage, M., & Thuan, T. X. 1992, *ApJ*, 396, L69
- Schawinski, K., Urry, C. M., Virani, S., et al. 2010, *ApJ*, 711, 284
- Schweitzer, M., Lutz, D., Sturm, E., et al. 2006, *ApJ*, 649, 79
- Shi, Y., Rieke, G. H., Hines, D. C., et al. 2006, *ApJ*, 653, 127
- Shi, Y., Ogle, P., Rieke, G. H., et al. 2007, *ApJ*, 669, 841
- Sikora, M., Stawarz, L., & Lasota, J.-P. 2007, *ApJ*, 658, 815
- Silverman, J. D., Lamareille, F., Maier, C., et al. 2009, *ApJ*, 696, 396
- Soifer, B. T., Helou, G., & Werner, M. 2008, *ARA&A*, 46, 201
- Soifer, B. T., Neugebauer, G., & Houck, J. R. 1987, *ARA&A*, 25, 187
- Storchi-Bergmann, T., González Delgado, R. M., Schmitt, H. R., Cid Fernandes, R., & Heckman, T. 2001, *ApJ*, 559, 147
- Sturm, E., Lutz, D., Verma, A., et al. 2002, *A&A*, 393, 821
- Tommasin, S., Spinoglio, L., Malkan, M. A., & Fazio, G. 2010, *ApJ*, 709, 1257
- Tommasin, S., Netzer, H., Sternberg, A., et al. 2012, *ApJ*, 753, 155
- Trujillo, I., Förster Schreiber, N. M., Rudnick, G., et al. 2006, *ApJ*, 650, 18
- Trump, J. R., Impey, C. D., Kelly, B. C., et al. 2011, *ApJ*, 733, 90
- Veilleux, S., & Osterbrock, D. E. 1987, *ApJS*, 63, 295
- Verma, A., Charmandaris, V., Klaas, U., Lutz, D., & Haas, M. 2005, *Space Sci. Rev.*, 119, 355
- Weedman, D. W., Hao, L., Higdon, S. J. U., et al. 2005, *ApJ*, 633, 706
- Whittle, M. 1992, *ApJS*, 79, 49
- Wright, E. L., Eisenhardt, P. R. M., Mainzer, A. K., et al. 2010, *AJ*, 140, 1868
- Wu, Y., Charmandaris, V., Huang, J., Spinoglio, L., & Tommasin, S. 2009, *ApJ*, 701, 658
- Xue, Y. Q., Brandt, W. N., Luo, B., et al. 2010, *ApJ*, 720, 368
- Yuan, F. 2007, in *Astronomical Society of the Pacific Conference Series*, Vol. 373, *The Central Engine of Active Galactic Nuclei*, ed. L. C. Ho & J.-W. Wang, 95